

## Changing Look AGN: An X-ray Look

Lev Titarchuk<sup>1</sup>, Elena Seifina<sup>2</sup> and Yegor Mishin<sup>2</sup>

### ABSTRACT

To date, a number of changing-look (CL) active galactic nuclei (AGNs) are known. We studied, in detail what happens to the X-ray spectrum during the CL events using the example of the nearby CL Seyfert NGC 1566, which was observed by *Swift*, *NuSTAR*, *XMM-Newton*, and *Suzaku*. We applied the Comptonization model to describe an evolution of NGC 1566 X-ray spectra during outbursts and compared these results with a typical behavior for other AGNs to identify some differences and common properties that can ultimately help us to better understand the physics of the CL phenomenon. We found that changes in the X-ray properties of NGC 1566 are characterized by a different combination of Sy1 (using 1H 0707–495 as a representative) and Sy2 properties (using NGC 7679 and Mrk 3 as their representatives). At high X-ray luminosities NGC 1566 exhibits the behavior typical for Sy1, and at low luminosities we see a transition of NGC 1566 from the Sy1 behavior to the Sy2 pattern. We revealed the saturation of the spectral indices,  $\alpha$  for these four AGNs during outbursts ( $\alpha_{1566} \sim 1.1$ ,  $\alpha_{0707} \sim 2$ ,  $\alpha_{7679} \sim 0.9$  and  $\alpha_{mrk3} \sim 0.9$ ) and determined the masses of the black holes (BHs) in the centers of these AGNs namely,  $M_{0707} \sim 6.8 \times 10^7 M_{\odot}$ ,  $M_{7679} \sim 8.4 \times 10^6 M_{\odot}$ ,  $M_{mrk3} \sim 2.2 \times 10^8 M_{\odot}$  and  $M_{1566} \sim 2 \times 10^5 M_{\odot}$ , applying the scaling method. Our spectral analysis shows that the changing-look of NGC1566 from Sy1.2 to Sy1.9 in 2019 was accompanied by the transition of NGC 1566 to an accretion regime which is typical for the intermediate and highly soft spectral states of other BHs. We also find that when going from Sy2 to Sy1, the spectrum of NGC 1566 shows an increase in the soft excess accompanied by a decrease in the Comptonized fraction ( $0.1 < f < 0.5$ ), which is consistent with the typical behavior of BH sources during X-ray outburst decay. Our results strongly suggest that the large diversity in

---

<sup>1</sup>Dipartimento di Fisica, Università di Ferrara, Via Saragat 1, I-44100 Ferrara, Italy, email:titarchuk@fe.infn.it; George Mason University Fairfax, VA 22030

<sup>2</sup>Moscow M.V. Lomonosov State University/Sternberg Astronomical Institute, Universitetsky Prospect 13, Moscow, 119992, Russia; seif@sai.msu.ru

its behavior observed among CL, Sy1, and Sy2 AGNs with different X-ray luminosities can be explained by changes in a single variable parameter, such as the ratio of the AGN’s X-ray luminosity to its Eddington luminosity, without any need for additional differences in Sy AGN parameters, such as its inclination, thereby blurring the distinction between the Sy1, Sy2 and CL-AGN subclasses.

*Subject headings:* accretion, accretion disks-black hole physics-stars:individual: 1H 0707–495, NGC 1566, NGC 7679, Mrk 3

## 1. Introduction

Recent detections of numerous changing-look active galactic nucleus (CL-AGN) events have led to a surge of interest in the study of this phenomenon. The origin of the CL-AGN events is still unclear. NGC 1566 galaxy is a prominent representative of the CL-AGN subclass of AGNs. Its supermassive black hole (SMBH) is estimated to be  $(1.3 \pm 0.6) \times 10^7 M_{\odot}$ . As the closest galaxy ( $z = 0.005$ , see also Table 1) among the CL-AGNs, NGC 1566 has been intensively studied over the past 70 years. It was first classified as a Seyfert 1 (Sy1) with the broad  $H_{\alpha}$  and  $H_{\beta}$  lines (de Vaucouleurs & de Vaucouleurs 1961). The  $H_{\beta}$  line was later found to be weak, leading to the source being classified as Seyfert 2 (Sy2) (Pastoriza & Gerola 1970). This is consistent with the generally accepted classification of AGN as Sy1 or Sy2, depending on the presence or absence of broad optical emission lines.

The existence of different classes of AGN can be explained using a unified model (Antonucci 1993), based on the orientation of an optically thick torus relative to the line of our vision. However, NGC 1566 exhibits the appearance or disappearance of broad optical emission lines, transitioning from Sy 2 (or Sy 1.8–1.9) to Sy 1 (or Sy 1.2–1.5) and vice versa within a few months (da Silva et al. 2017), and does not fit into the generally accepted classification and constitutes a significant problem in our understanding of AGN.

Since 2018, observations of NGC 1566 have been carried out in many wavelength ranges: from hard X-rays (see X-ray image of NGC 1566 in Fig. 2) to infrared rays (Ducci et al. 2018). It became clear that the NGC 1566 flux varies in all wavelengths. In particular, in July 2018, its flux increased strongly and reached its peak (Parker et al. 2019; Oknyansky et al. 2019, 2020). Long-term light curves of ASAS-SN and NEOWISE showed that the IR and optical flux began to increase as early as September 2017 (Cutri et al. 2018; Dai et al. 2018). The Swift/XRT flux increased by about 30 times (Fig. 1) when the source changed from Sy1.8–1.9 to Sy1.2 (Oknyansky et al. 2020, 2019). The source became Sy1 with an appearance of strong broad emission lines (Oknyansky et al. 2019; Ochmann et al. 2020). Having reached their peak, the source fluxes



decreased in all wavebands. Several smaller flares were observed after the main outburst (Grupe et al. 2018, 2019).

This 2018–2019 outburst of NGC 1566 with a CL-effect was observed using *NuSTAR* and *XMM-Newton*. Jana et al. (2021) investigated these observations applying the power-law, NTHCOMP, OPTXAGNF and RELXILL models with an addition of Gaussian lines and taking into account X-ray absorption effects. Each of these models shed light on the CL-peculiarities and the change in the object itself. In the power-law model, Jana et al. (2021) found the presence of a soft excess ( $< 2$  keV), which they approximated by an additional bbody component. This model fits well the *XMM-Newton* data for about 2.5 years before the 2018 outburst with parameters  $N_H = (3.53 \pm 0.06) \times 10^{21} \text{ cm}^{-2}$  and a photon index  $\Gamma \sim 1.7$  ( $\Gamma = \alpha - 1$ ). Moreover, an iron  $K_\alpha$  emission line was detected at 6.4 keV with an equivalent width (EW) of 200 eV. The rise phase of the 2018 outburst was analyzed using simultaneous *XMM-Newton* and *NuSTAR* observations of NGC 1566, and in this model the fit yielded  $\Gamma = 1.8$ .

The Fe  $K_\alpha$  line was detected at 6.38 keV with an  $EW > 110$  eV, as well as the Fe XXVI emission feature at 6.87 keV with an  $EW < 37$  eV. It is interesting to note that two ionized absorbers were required to fit the source spectra in the rise phase, one low-ionization absorber ( $\xi \sim 101.7 \pm 0.1$ ) with  $N_{H,1} = (8.1 \pm 2.2) \times 10^{20} \text{ cm}^{-2}$ , and one high-ionization absorber ( $\xi \sim 104.7 \pm 0.4$ ) with  $N_{H,2} = (4.3 \pm 0.4) \times 10^{21} \text{ cm}^{-2}$ .

In the outburst decay phase the photon index was almost constant ( $\Gamma \sim 1.7$ ), the blackbody temperature was constant  $kT_{bb} \sim 110$  eV and the Fe  $K_\alpha$  line was detected with  $EW > 100$  eV. Although column density of the weakly ionizing absorber varied in the range of  $N_{H,1} \sim (1.2 - 1.3) \times 10^{21} \text{ cm}^{-2}$ , no highly ionizing absorber was required to fit the spectra during the outburst decay. In addition, a weak reflection hump was detected as an excess of emission at energies 15–40 keV. In the NTHCOMP model, Jana et al. (2021) fixed the seed photon temperature at  $kT_s = 30$  eV. They again needed to account for two absorption components during the outburst rise and initial decay phases. They found that as the corona size  $R_{cor}$  decreased, the plasma electron temperature  $kT_e$  increased from 60 to 100 keV with a nearly constant photon index ( $\Gamma = 1.7 - 1.9$ ).

To model this NGC 1566 outburst with OPTXAGNF Jana et al. (2021) again accounted for two absorption components during the outburst rise and initial decay phases. The photon index  $\Gamma$  and optical depth  $\tau$  were held almost constant at  $\Gamma = 1.7 - 1.8$  and  $\tau \sim 4 - 5$  throughout the 2018 outburst. Before this outburst, the Eddington ratio and the size of the X-ray corona were found to be small ( $L/L_{Edd} \sim 0.04$  and  $R_{cor} = 12R_g$ ) compared to the rise phase outburst ( $L/L_{Edd} \sim 0.23$  and  $R_{cor} = 43R_g$ ). In later observations, they decreased  $L/L_{Edd} \sim 0.06$  and  $R_{cor} \sim 20R_g$ .

This model fit all observations well and indicated an increase in the accretion rate and corona size at the outburst peak, as well as a high degree of the plasma Comptonization during the outburst.

The RELXILL model again required taking into account two absorption components during the rising and initial decay phases of the outburst. In addition, the model included the reprocessed X-ray emission from the disk as a reflectivity parameter  $R_{refl}$ , which turned out to be relatively weak ( $R_{refl} \sim 0.1 - 0.2$ ) throughout the outburst. The inner disk edge  $R_{in}$  varied from  $4R_g$  to  $7R_g$ .

Tripathi & Dewangan (2022a), hereafter TD22a also analyzed NGC 1566 using *XMM-Newton*, *Swift* and *NuSTAR* data at different epochs during the decay phase of the 2018 outburst using a broadband continuum model OPTXAGNF (Done et al. 2012) taking into account the thermal Comptonization (THCOMP) and the reflection (RELXILL) model, as well as investigated the correlations between the accretion disk X-ray emission, soft X-ray excess and the power-law continuum. They argued that at low X-ray flux levels, the source soft X-ray excess was absent and only the disk emission provided seed photons for thermal Comptonization in the corona, while at high flux levels, both the soft X-ray excess and the disk emission were present, providing seed photons for the thermal Comptonization in the corona.

TD22a found that the X-ray photon index remained constant ( $\Gamma \sim 1.66 - 1.72$ ), although the electron temperature of the corona increased from 22 to 200 keV from June 2018 to August 2019. At the same time, the optical depth of the corona  $\tau$  decreased from 4 to 0.7, and the scattering fraction increased from 1% to 10%. TD22a interpreted this as an increase in the size of the corona and its heating with a decrease in the mass accretion rate during the decay phase.

Different models are used to study AGN, including those specifically designed for AGN (assuming a specific structure of active galactic nuclei) and generalized models (with a minimum number of specific assumptions). The first of these, such as the AGNSED model (Kubota & Done 2018) and models taking into account the double (warm and hot) corona (Petrucci et al. 2013), consider three zones of AGN X-ray formation: an outer standard disc, an inner warm Comptonizing region (to produce the soft X-ray excess) and a hot corona (see Fig. 10 in Petrucci et al. (2013)). Generalized models such as the BMC (Titarchuk et al. 1997; Titarchuk & Zannias 1998; Laurent & Titarchuk 1999; Borozdin et al. 1999; Shrader & Titarchuk 1996), NTHComp (Zdziarski et al. 1996), Comptb (Farinelli & Titarchuk 2011), Comptt (Titarchuk 1994) are based on the first principles and also consider three X-ray formation regions: an outer standard disc, a hot Comptonizing region (a so called *Transition layer*) to reproduce the soft X-ray excess and a thermal Comptonization hump in the source spectrum, and a converging flow region (possibly analogous to a hot corona, to form a hard high-energy tail in the source X-ray spectrum). In this paper, we apply these generalized models to identify the features of CL-AGN compared to Sy1 and Sy2, without assuming a specific geometry of these sources.

In addition, for better understanding the properties of NGC 1566 during CL events, it is interesting to compare the behavior of this CL-AGN with other AGNs, such as Sy1 and Sy2. To do this, we used the Sy1 galaxy (1H 0707–495) and the Sy2 galaxy (NGC 7679) to study their

differences and similarities during X-ray outbursts in comparison to CL-AGN.

The Narrow-Line Sy 1 galaxy 1H 0707–495 ( $z = 0.0411$ , hereafter 1H 0707, see also Table 1) is a bright Narrow Line Seyfert 1 (NLS1) galaxy (Leighly 1999). BH mass estimates in 1H 0707 vary over a wide range from  $2 \times 10^6$  to  $10^7 M_\odot$  Zhou & Wang (2005); Kara et al. (2013); Done & Jin (2016). In particular, Zoghbi et al. (2011) assumed that most of the radiation is emitted at  $\sim 2r_g$  and estimated the inner radius and the emissivity index using their spectral fitting. They interpreting the 30 s lag as the light crossing time and estimated a BH mass of  $M_{BH} \sim 2 \times 10^6 M_\odot$ , which was consistent with the uncertain mass of this BH quoted in the literature (Zhou & Wang 2005).

NGC 7679 is a barred lenticular galaxy seen face on (Yankulova et al. 2007). It is located at a distance of about 200 million light years from Earth (see also Table 1). It was discovered by Heinrich d’Arrest on September 23, 1864. The nucleus of NGC 7679 turned out to be active and was classified as a Seyfert galaxy. The most common theory for the energy source of Seyfert galaxies is the presence of an accretion disk around a supermassive black hole. NGC 7679 is believed to host a supermassive black hole, with a mass estimated at  $5.9 \times 10^6 M_\odot$  based on velocity dispersion (Alonso-Herrero et al. 2013). The X-ray spectrum of NGC 7679 using *BeppoSAX* shows no significant absorption above 2 keV, and the  $K_\alpha$  line of iron was only slightly detected. However, the galaxy shows signs of obstruction to visual light as it lacks broad emission lines. Two possible reasons: the presence of dust or an X-ray emitting accretion disk that is not covered and the broad line region is covered (Risaliti 2002a). To date, the classification of NGC 7679 as Sy1 or Sy2 remains controversial. On the one hand, this AGN has an optical spectrum without broad emission lines, which allows it to be classified as a Sy2 (Risaliti 2002a). On the other hand, NGC 7679 has significant variable X-ray emission, typical of Sy1. The main feature of objects like NGC 7679 is not the strength of their starburst, but the apparent optical faintness of the Sy1 nucleus when compared to the X-ray luminosity.

As a second representative of Sy2 galaxies we used Markarian 3 (hereafter Mrk 3), which is one of the brightest and best-studied members of the Sy2 class. The host galaxy is classified as an elliptical or *S0* galaxy type. Awaki et al. (1990), Awaki et al. (1991) and Smith & Done (1996) revealed an anomalously flat power-law continuum emerging through a tall occultation column ( $N_H \sim 6 \times 10^{23} \text{ cm}^{-2}$ ) from *GINGA* observations of Mrk 3. A strong Fe line with high equivalent width ( $EW \sim 1.3 \text{ keV}$ ) was also detected. Mrk 3 has the hardest spectrum among all 16 Sy2 galaxies studied by Smith & Done (1996), significantly harder than the spectrum of Sy1 galaxies. In *ASCA* observations of Mrk 3, the object showed a spectrum with a photon index  $\Gamma \sim 1.8$  and a two-component iron line (Iwasawa et al. 1994).

Thus, the dominant component of the  $K_\alpha$  iron line at 6.4 keV has  $EW = 0.9 \text{ keV}$ , while the second component at 7 keV has  $EW = 0.2 \text{ keV}$ . A reanalysis of the spectrum of Mrk 3 using

non-simultaneous *GiNGA*, *ROSAT* and *ASCA* observations (Griffiths et al. 1998) covering a wide spectral band (0.1–30 keV) yielded a typical value for the power law,  $\Gamma \sim 1.7$ , when either an additional absorption edge at 8 keV (possibly arising from a warm absorber) or reflection was included in the spectral model. Recent observations with *BeppoSAX* (Cappi et al. 1999), which extend the spectral coverage to 150 keV, indeed confirm a presence of a steep ( $\Gamma \sim 1.8$ ) internal power law. Turner et al. (1997) also reanalyzed the *ASCA* data and proposed an alternative model in which the internal continuum is resolved through very large absorption column ( $N_H > 10^{24} \text{ cm}^{-2}$ ), while the reflection component is not obscured.

Georgantopoulos et al. (1999) analyzed the *RXTE* data for Mrk 3 and found an agreement with the earlier results of *GiNGA*. They used a spectral model consisting of a very hard power-law continuum ( $\Gamma \sim 1.1$ ) modified below  $\sim 6$  keV by a strongly absorbing column ( $N_H \sim 6 \times 10^{23} \text{ cm}^{-2}$ ) and an iron line with a high equivalent width at 6.4 keV. Their conclusions are consistent with the results by Turner et al. (1997) on the complex absorption of a molecular torus.

It is interesting to note that Boorman et al. (2018) found an anti-correlation between the equivalence width of the narrow core of the neutral Fe  $K\alpha$  fluorescence line, ubiquitously observed in the reflection spectra of obscured AGNs, and the mid-infrared continuum luminosity at  $12 \mu\text{m}$ . This is consistent with numerous studies of the X-ray Baldwin effect for unobscured and slightly obscured AGNs and challenges the traditional view that the Fe  $K\alpha$  line originates from the same region as the underlying reflection continuum, which together make up the reflection spectrum. However, the found anti-correlation does not apply to Mrk 3, as Ricci et al. (2015) find a Compton-thin column density (90% confidence level) for this source.

Risaliti (2002b) discuss another type of X-ray changing look for AGNs based on changes in column density (from 20% to 80%) during AGN X-ray variability on time scales of months to years. Namely, the AGN switched between thin Compton thin ( $N_H < 1.5 \times 10^{24} \text{ cm}^{-2}$ ) and Compton thick ( $N_H > 1.5 \times 10^{24} \text{ cm}^{-2}$ ) regimes (see also Matt et al. (2003)).

To describe the BH states in AGN during outbursts, it is convenient to use the terminology used to identify the BH states in X-ray binaries (XRBs). Thus, the observed manifestations of BHs in galactic sources are traditionally described in terms of a classification of BH spectral states (see Klein-Wolt & van der Klis (2008); Remillard & McClintock (2006); Belloni et al. (2005), for various definitions of BH states). A general classification of BH states for four main BH states is accepted by the community: the quiescent, the low hard (LHS), the intermediate (IS, sometimes subdivided into Hard intermediate, HIMS, and Soft intermediate, SIMS) and the high soft (HSS) states.

When a BH transient goes into an outburst, it leaves the quiescent state and enters the LHS, a low-luminosity state with an energy spectrum dominated by the thermal component of Comp-

tonization combined with a weak thermal component. The photon spectrum in the LHS is thought to be the result of Comptonization (upward scattering) of soft photons, which originated in the relatively weak inner part of the accretion disk, from electrons in the hot surrounding plasma (see, e.g., Sunyaev & Titarchuk (1980)). The HSS photon spectrum is characterized by a pronounced thermal component, which is probably a sign of strong radiation emanating from the geometrically thin accretion disk. The IS is a transition state between the LHS and the HSS. At the same time, the subdivision the IS into SIMS and HIMS states reflects the specifics of a BH source at the entrance and exit from the outburst. As for supermassive BHs in AGNs, despite the different time scale, sizes and sources of accreted matter compared to XRBs, they show a similar pattern of the spectral changes during their outbursts. Therefore, we use the terminology given above, but note that there is, of course, no direct analogy. In addition, the excess soft radiation of AGNs is another component of the Comptonization effect, since the disk temperature of AGNs is much lower.

X-ray spectroscopy is a very powerful tool for shedding light on the CL-AGN relationship, mainly because X-rays are emitted closer to the primary emission source than optical emission lines, which are reprocessed emission from interstellar gas (e.g., Terashimai et al. (2009)). In this paper we present the comparative analysis for NGC 1566, 1H 0707–495 and NGC 7679 using the *Suzaku*, *ASCA*, *Swift* and *BeppoSAX* observations. In §2 we present the list of observations used in our data analysis while in §3 we provide the details of X-ray spectral analysis. We analyze an evolution of X-ray spectral and timing properties during the state transition in §4. In §5 we present a description of the spectral models used for fitting these data. In §6 we discuss the main results of the paper. In §7 we present our final conclusions.

## 2. Data Selection

NGC 1566 was observed by *Swift* (2007–2023) and with *Suzaku* (2012). 1H 0707–495 was detected by *Swift* (2010–2018), by *ASCA* (1995, 1998 and 2005) as well as with *Suzaku* (2005). While NGC 7679 was observed by *Swift* (2017 and 2019), by *ASCA* (1998 and 1999) and with *BeppoSAX* (1998). We extracted these data from the HEASARC archives and found that these data cover a wide range of X-ray luminosities (see Tables 2 and 3). We recognized that the well-exposed *BeppoSAX*, *ASCA* and *Suzaku* data are preferable for the determination of low-energy photoelectric absorption.

## 2.1. *Swift data*

Using *Swift*/XRT data in the 0.3–10 keV energy range, we studied flaring events of NGC 1566, 1H 0707 and NGC 7679 (see the log of observations for all three sources in Table 3). The data used in this paper are public and available through the GSFC public archive<sup>1</sup>.

Data were processed using the HEASOFT v6.14, the tool `xrtpipeline` v0.12.84, and the calibration files (CALDB version 4.1). The ancillary response files were created using `xrtmkarf` v0.6.0 and exposure maps were generated by `xrtexpomap` v0.2.7. The source events accumulated in a circular region of optimal radius from 17 to 45" centered on the individual source position shown in Table 1. The background was estimated in a nearby source-free circular region taking into account the relative areas of the source and background regions. Spectra were rebinned with at least ten counts in each energy bin using the `grppha` task in order to apply  $\chi^2$  statistics. We also used the online XRT data product generator<sup>2</sup> to obtain the image of the source field of view in order to make a visual inspection and to get rid of possible contamination by nearby sources (Evans et al. 2007, 2009).

## 2.2. *BeppoSAX data*

We used *BeppoSAX* data of NGC 7679 carried out on December 6–9, 1998. In Table 2 (bottom line) we show the log of the *BeppoSAX* observation analyzed in this paper. Generally, broad band energy spectra of the source were obtained combining data from three *BeppoSAX* Narrow Field Instruments (NFIs): the Low Energy Concentrator Spectrometer [LECS; Parmar et al. (1997)] for 0.3 – 4 keV, the Medium Energy Concentrator Spectrometer [MECS; Boella et al. (1997)] for 1.8 – 10 keV and the Phoswich Detection System [PDS; Frontera et al. (1997)] for 15 – 60 keV. The SAXDAS data analysis package is used for processing data. For each of the instruments we performed the spectral analysis in the energy range for which the response matrix is well determined. Both LECS and MECS spectra were accumulated in circular regions of 4' radius. The LECS data have been re-normalized based on MECS. Relative normalization of the NFIs were treated as free parameters in model fitting, except for the MECS normalization that was fixed at a value of 1. We checked after that this fitting procedure if these normalizations were in a standard range for each instruments<sup>3</sup>. In addition, spectra are rebinned accordingly to energy resolution of the instruments in order to obtain significant data points. We rebin the LECS spectra

---

<sup>1</sup><https://heasarc.gsfc.nasa.gov>

<sup>2</sup>[http://www.swift.ac.uk/user\\_objects/](http://www.swift.ac.uk/user_objects/)

<sup>3</sup><http://heasarc.nasa.gov/docs/sax/abc/saxabc/saxabc.html>

with a binning factor which is not constant over energy (Sect.3.1.6 of Cookbook for the BeppoSAX NFI spectral analysis) using re-binned template files in GRPPHA of XSPEC<sup>4</sup>. Also we re-binned the PDS spectra with linear binning factor 2, grouping two bins together (resulting bin width is 1 keV). Systematic error of 1% have been applied to these analyzed spectra.

### 2.3. *Suzaku* data

*Suzaku* observed NGC 1566 and 1H 0707. Table 2 summarizes the start and end times, and the MJD interval for each of these observations, indicated by *green* triangle in top of Figure 1 for NGC 1566. One can see a description of the *Suzaku* experiment in Mitsuda et al. (2007). For observation obtained by a focal X-ray CCD camera (XIS, X-ray Imaging Spectrometer, Koyama et al. (2007)), which is sensitive over the 0.3–12 keV range, we used software of the *Suzaku* data processing pipeline (ver. 2.2.11.22). We carried out the data reduction and analysis following the standard procedure using the HEASOFT software package (version 6.25) and following the *Suzaku* Data Reduction Guide<sup>5</sup>. The spectra of the source were extracted using spatial regions within the 3.51'-radius circle centered on the source nominal position (Table 1), while a background was extracted from source-free regions for each XIS module separately.

The spectrum data were re-binned to provide at least 20 counts per spectral bin to validate the use of the  $\chi^2$ -statistic. We carried out spectral fitting applying XSPEC v12.10.1. The energy ranges around of 1.75 and 2.23 keV are not used for spectral fitting because of the known artificial structures in the XIS spectra around the Si and Au edges. Therefore, for spectral fits we have chosen the 0.3 – 10 keV range for the XISs (excluding 1.75 and 2.23 keV points).

### 2.4. *ASCA* data

*ASCA* observed 1H 0707–495 and NGC 7679 (see Table 2, which summarized the start time, end time, and the MJD interval. One can see a description of the *ASCA* data by Tanaka et al. (1994). The solid imaging spectrometers (SIS) operated in Faint CCD-2 mode. The *ASCA* data were screened using the ftool ascascreen and the standard screening criteria. The spectrum for the source were extracted using spatial regions with a diameter of 4' (for SISs) and 6' (for GISs) centered on the nominal position of the source, while background was extracted from source-free regions of comparable size away from the source. The spectrum data were re-binned to provide

---

<sup>4</sup><http://heasarc.gsfc.nasa.gov/FTP/sax/cal/responses/grouping>

<sup>5</sup><http://heasarc.gsfc.nasa.gov/docs/suzaku/analysis/>

at least 20 counts per spectral bin to validate the use of the  $\chi^2$ -statistic. The SIS and GIS data were fitted using XSPEC in the energy ranges of 0.6 – 10 keV and 0.8 – 10 keV, where the spectral responses are well-known.

## 2.5. *RXTE* data

We have also analyzed the available data of 1H 0707–495 (1997) obtained with *RXTE* (Bradt et al. 1993). We have made an analysis of the *RXTE* observation of 1H 0707 during *the low/hard state*, *LHS* (ID=20309-01-01-00). We should note that the "LHS", "HSS" notations, are not very often applied to AGNs. Altogether, we introduce these notations because of the photon index change  $\Gamma$ . For example, in similarity with binary systems if the  $\Gamma$  index is within the 1.5-1.7 range then we associate it with the Comptonization photon index which is typical for the low/hard spectrum in the binaries and vice versa if  $\Gamma > 2.3$  then we relate it with the high/soft state (HSS) observed in the binaries.

Standard tasks of the LHEASOFT/FTOOLS 6.33.2 software package were utilized for data processing using methods recommended by *RXTE* Guest Observer Facility according to the *RXTE* Cook Book<sup>6</sup>. For spectral analysis, we used data from the Proportional Counter Array (PCA) and High-Energy X-Ray Timing Experiment (HEXTE) detectors. *RXTE/PCA* spectra (*Standard 2* mode data, 3 – 50 keV energy range) have been extracted and analyzed using the PCA response calibration (ftool pcarmf v11.1). The relevant deadtime corrections to energy spectra have been applied. In turn, HEXTE data in the 20–150 keV energy range were used for the spectral analysis in order to exclude the channels with largest uncertainties. We subtracted background corrected in off-source observations.

We used the data which are available through the GSFC public archive<sup>7</sup>. In Table 2 we presented the informations of the *RXTE* observation of 1H 0707 and Mrk 3. Systematic error of 0.5% have been applied to the analyzed spectrum.

---

<sup>6</sup>[http://heasarc.gsfc.nasa.gov/docs/xte/recipes/cook\\_book.html](http://heasarc.gsfc.nasa.gov/docs/xte/recipes/cook_book.html)

<sup>7</sup><http://heasarc.gsfc.nasa.gov>



## 2.6. *NuSTAR* data

We processed *NuSTAR* observations using the NuSTARDAS (version 2.1.1) and the latest files available in the *NuSTAR* Calibration Database <sup>8</sup>. We generated clean event files for each observation of NGC 1566 using the *nupipeline* task and extracted the source and background spectra from circular regions of 60" and 90" radius, respectively, centered at the source position (Table 1). Source spectra were extracted using the *nuproduct* task. We binned each spectrum so that there were at least 25 counts per spectral bin.

## 2.7. *XMM–Newton* data

We processed the *XMM–Newton* data from EPIC-pn (Struder et al. 2001) using SAS software (version 18.0.0)<sup>9</sup> and the latest calibration files. Following Jana et al. (2021), we corrected for the pile-up by excluding events in the inner 10" radius circular region from the clean event lists. We extracted the source spectrum from the annular region (with outer radius 30" and inner radius 10"<sup>10</sup>) centered at the source position (Table 1) and the background spectrum from a 40" radius circular region from the source-free region for each observation. The response files (*arf* and *rmf* files) were generated using the SAS *arfgen* and *rmfgen* tasks, respectively. We binned each spectrum so that there were at least 25 counts per spectral bin.

# 3. Results

## 3.1. Images of NGC 1566, 1H 0707–495, NGC 7679 and Mrk 3

The *Swift*/XRT (0.3 – 10 keV) image of the NGC 1566, 1H 0707–495, Mrk 3 and NGC 7679 fields of view (FOVs) are presented in Figs. 2–5, respectively.

*Swift* X-ray image of NGC 1566 (Fig. 2) is accumulated from 12th December, 2007 to 1 November 2023 with an exposure time of 230 ks. Yellow contours in this image demonstrate the lack of X-ray jet structure (elongated), as well as minimal contamination by other point sources within 18" in the field of view around NGC 1566. The closest next source is 21" (LSXPS J041956.5–545528 is marked with a green circle).

---

<sup>8</sup><http://heasarc.gsfc.nasa.gov/FTP/caldb/data/nustar/fpm/>

<sup>9</sup><https://www.cosmos.esa.int/web/xmm-newton/sas-threads>

<sup>10</sup><https://www.cosmos.esa.int/web/xmm-newton/sas-thread-epatplot>

The field of view for 1H 0707 is shown in Fig. 3. *Swift* X-ray image of 1H 0707–495 (2SXPS J070841.4–493306 – according to the *Swift* catalog), accumulated from April 3, 2010 to April 30, 2018 with a 161 ks exposure time. The gray dashed square with a side of 6.3' (160 pixels) in the 1H 0707 image demonstrates the absence of other nearby objects in the 1.3' field of view. The next closest source is 2.8' away (outside the image).

According to the *Swift* catalog), the field of view for Mrk 3 is shown in Fig. 4. *Swift* X-ray image of Mrk 3 (2SXPS J061536.2+710214 accumulated from May 3, 2006 to April 20, 2015-04-20 with a 91 ks exposure time. The green contours in this image demonstrate the lack of X-ray jet-like structure around Mrk 3, as well as minimal contamination by other point sources within 18" of the source environment. The closest next source is 21" (LSXPS J041956.5–545528 is marked with a white circle, see Fig. 4).

The *Swift* X-ray image of NGC 7679, presented in Fig. 5, is catalog), accumulated from July 25, 2015 to October 6, 2017 with a 1.7 ks exposure time. The image segment highlighted with a gray square (6.3' to a side) is also shown in more detail in the enlarged panel. Contour levels demonstrate the absence of X-ray jet (elongated) structure and minimal contamination from other point sources and diffuse radiation in the 1.3' field of view around NGC 7679. The next closest source, 279" is 2LSXPS J232904+032910.

### 3.2. X-ray Light Curves

All three sources are Seyfert galaxies and the BHs at their centers have approximately the same masses ( $\sim 10^6 M_{\odot}$ , see Table 1). However, they exhibit completely different temporal patterns of activity. To demonstrate this, we compared their long-term behavior in the form of light curves.

#### 3.2.1. NGC 1566 Light Curve

We present a long-term X-ray light curve of NGC 1566 detected by the XRT on board of *Swift* from 2007 – 2023 (see Fig. 1). In addition, we used *Suzaku* data from this AGN and marked the time of its observations with a green arrow in the background of the *Swift* light curve (in top panel). In the bottom panel of this figure, we have presented the optical light curve by *Swift*/UVW2 [1600–2230 Å] (hazel stars) and by *Swift*/BAT [15–50 keV] (black dots) observations to trace the quiet/active states of NGC 1566 at different wavelengths. Figure 1 also shows that NGC 1566 was in the LHS state from 2007 to 2017.

Here, along with the countrate light curve in total band [0.3–10 keV], it is also interesting to

investigate the hardness count-rate light curves without using any model. Thus, we study the light curve of NGC 1566 with a bintime of 1 ks for four energy bands 0.3–10 keV, 0.3–1 keV, 1–2 keV and 3–10 keV. Using these energy-dependent light curves, the soft hardness coefficient ( $HR1$ ) is defined as the ratio of the difference in count rates in the 1–2 keV ( $M$ ) and 0.3–1 keV ( $S$ ) energy bands to their sum, and the hardness coefficient ( $HR2$ ) is defined as the ratio of the difference in count rates in the 2–10 keV ( $H$ ) and 1–2 keV ( $M$ ) energy bands to their sum (see recommendations in 2SXPS<sup>11</sup>):  $HR1 = (M - S)/(M + S)$  and  $HR2 = (H - M)/(H + M)$ . In this approach, NGC 1566 shows variability in terms of  $HR1$  (blue points) and  $HR2$  (pink points) during transient events from 2007 to 2023 (see second panel from top in Fig. 6). From 2017 to 2019, the object entered an active state with a powerful outburst, followed by decay, accompanied by a series of repeated re-flares of smaller amplitude. Comparison of the top and bottom panels of Fig. 6 demonstrate that the source light curves in the optical (UVW2) and X-ray (Swift/XRT and Swift/BAT) ranges correlate quite well. Around this time a changing-look of the galaxy occurred. It can be seen that during the changing-look events (marked by vertical blue stripes,  $F1 - F4$ ) NGC 1566 was characterized by the dominance of the soft component, and only after the outburst peak, a softening of its spectrum occurred during repeated small flares (MJD 58,400–59,000,  $F2 - F3$ ) during the decay phase. So this interval is most interesting for subsequent spectral analysis (see Sect. 3.3).

### 3.2.2. 1H 0707 Light Curve

The light curve of Sy1 galaxy 1H 0707 is shown in Fig. 7 before, during, and after the transient events from 2010 to 2018. It can be seen that in 2011 (MJD 55550–65599) 1H 0707 remained in the stable low/hard state (mean countrate  $\sim 0.02$  cnt/s). During the rest of the *Swift* observations, the object is highly variable.

Overall, 1H 0707 shows four X-ray outbursts (marked with vertical blue strips) with good coverage of the rise-peak-decay in our sample (see Table 3). Furthermore, the object shows variability in terms of  $HR1$  (blue dots) and  $HR2$  (pink dots) during transient events with a clear dominance of source hard emission from 2010 to 2018 (Fig. 9).

### 3.2.3. NGC 7679 Light Curve

The Sy2 galaxy NGC 7679 has a modest monitoring history and, according to optical observations (see Fig. 10 from Catalina Sky Survey (CSS, V-band, blue dots), the object is weakly

---

<sup>11</sup><https://heasarc.gsfc.nasa.gov/W3Browse/swift/swift2sxps.html>

variable, at least in the V band. In Fig. 10 we also show the time distribution of observations of NGC 7679 using ASCA (grey arrows), *BeppoSAX* (green arrow) and *Swift*/XRT (bright blue vertical strip with red points) in conjunction with the source optical light curve in V band. Apparently, *Swift*/XRT detected an X-ray flare from NGC 7679 around MJD 58033.

### 3.2.4. *Mrk 3 Light Curve*

The light curve of Sy2 galaxy Mrk 3 is shown in Fig. 11 before, during, and after the transient events from 2010 to 2018. From this figure we can see that in early 1996 (MJD 50450–50520) Mrk 3 remained in a stable low/hard state (average count rate  $\sim 2 - 3$  cnt/s). Then two outbursts occurred around MJD 50540 and 50550, when the count rate increased to 5 cnt/s. During the rest of the *RXTE* observations the object remained in a stable low/hard state.

Generally, Mrk 3 shows two X-ray outbursts (marked with vertical blue strips) in our sample (see Table 2). Furthermore, the object shows variability in X-ray fluxes in 3–10 keV (blue dots) and 10–20 keV (pink dots) bands during transient events with a clear dominance of source hard emission from 1996 to 1997 (Fig. 9).

## 3.3. Spectral Analysis

### 3.3.1. *Model Selection*

To model AGN spectra, special models such as AGNSED (Kubota & Done 2018) and dual-coronal (Petrucci et al. 2013) are created. In fact, they take into account the specific geometry of AGNs with a breakdown into an outer standard disc, an inner warm Comptonization region and a hot corona (Kubota & Done 2018). The last two components are called warm and hot corona (dual-coronal model by Petrucci et al. (2013)), which are described by the thermal Comptonization with different plasma temperatures. Petrucci et al. used mainly the warm corona component to describe the soft X-ray excess in the AGN spectra in the low/hard state (see also the discussion in Sect. 4).

Titarchuk et al. (1994-2024) in their papers indicate that the generalized Comptonization model called XSPEC BMC [the *Bulk Motion Comptonization* is a XSPEC Comptonization by relativistic matter model<sup>12</sup>] can be applied to any state and Comptonization type (thermal or dynamic) for the observed X-ray spectra of BHs or NSs (Titarchuk et al. 2024, 2023; Titarchuk and Seifina 2023, 2021; Titarchuk et al. 2020; Titarchuk and Seifina 2017, 2016a,b; Titarchuk et al. 2014,

---

<sup>12</sup><https://heasarc.gsfc.nasa.gov/xanadu/xspec/manual/node142.html>

2010; Titarchuk and Seifina 2009) . Thus, we apply the BMC model as a generalized one for all AGN sources in all spectral states. The BMC model calculates the soft excess and the primordial emission self-consistently. In this model, the total emission is determined by the BMC normalization  $N_{bmc}$ , which is proportional to the mass accretion rate and the spectral index  $\alpha$  (or the photon index  $\Gamma = \alpha + 1$ ). The disk emission appears as a color temperature-corrected blackbody emission at radii  $R_{out} > r > R_{TL}$ , where  $R_{out}$  and  $R_{TL}$  are the outer disk radius and the outer radius of the transition layer (TL), respectively. At  $r < R_{TL}$ , the disk emission appears as the Comptonized emission from the warm and optically thick medium, rather than as the thermal one. The hot and optically thin TL is located in the inner part of the disk around the BH ( $R_{TL} < r < R_{ISCO}$ , where  $R_{ISCO}$  is the radius of the last stable orbit) and creates a high-energy power-law continuum. The total Comptonized radiation is split between the (hot) TL and the (cold) BH-converging flux (CF, where dynamical Comptonization is effective), and the fraction of (hot) Comptonized radiation ( $f$  or  $logA$ ) can be found from a model fit. The seed photon temperature ( $kT_s$ ) and the TL spectral index of the corona determine the energy of the upward-scattered soft excess radiation. The Compton continuum is approximated as a convolution of the BB blackbody radiation with the Comptonization Green function  $G$ , which can be described as

$$G(x, x_0) = x^{-\alpha}, \quad \text{if } x > x_0, \quad (1)$$

$$G(x, x_0) = x^{\alpha+3}, \quad \text{if } x < x_0, \quad (2)$$

where  $x = hv/kT_e$ ,  $x_0$  is the breakpoint of  $G(x, x_0)$  at the point where the two cases ( $x > x_0$  and  $x < x_0$ ) meet each other. Thus, the general model consists of a BBody-like and a Comptonized component (XSPEC models “BMC”, “COMPTB”, “COMPTT” are the sum of these components:  $BB + f \cdot BB * G$ ). When using the BMC model, we included a Gaussian component to account for the Fe emission lines. The model reads in XSPEC as `tbabs * (BMC+Gaussian)`. For all sources we used the Comptonization model BMC modified (see the description of the model in Fig. 8) by neutral absorption and the *Gaussian* line at  $\sim 6.5$  keV. The parameters of a *Gaussian* component are a centroid line energy  $E_{line}$ , the width of the line  $\sigma_{line}$  and normalization,  $N_{line}$  to fit the data in the 6 – 8 keV energy range. We also use interstellar absorption with a column density  $N_H$  (see Table 1).

As for the inclusion of the iron line in the source spectrum fitting model for 1H 0707, some explanations should be given here. The first time the iron fluorescent line in 1H 0707–495 was detected by Fabian et al. (2009) using *XMM-Newton*. The previous observations showed only a sharp and deep drop in the spectrum at 7 keV, but did not reveal narrow emission features. This has given rise to two interpretations (Boller et al. 2002): either the source is partially shielded by a large layer of iron-rich material (then the sharp drop is due to a photoelectric absorption edge), or it has very strong X-ray reflection (Fabian et al. 2004) in its innermost regions, where relativistic

effects change the observed spectrum (the sharp drop in the spectrum by energy 7 keV is due to the blue wing of the line (see also Seifina (1999)), partly formed by relativistic Doppler shifts).

Absorption requires the iron abundance to be about 30 times the solar value, while reflection requires this ratio to be between 5 and 10. Fabian et al. (2009) showed that the extreme variability in the soft range of the 1H 0707 spectrum does not make sense in the model partial coverage. However, analysis of the spectral variability of the source showed the spectrum of the source in all states (low and high flux) to be well described by a power-law continuum with a photon index  $\Gamma = 3$ , with an excess at lower energies ( $\leq 1.1$  keV). Fabian et al. (2009) argued that the 1H 0707 spectra are well described by a simple phenomenological model consisting of a power-law continuum, a soft blackbody, two relativistically broad *Laor* lines (Laor 1991) and galactic absorption (corresponding to  $N_H = 5 \times 10^{20} \text{ cm}^{-2}$ ). These lines are characterized by energies of 0.89 and 6.41 keV (in the rest frame), an innermost radius of  $1.3R_g$  ( $R_g = GM_{BH}/c^2$ , wherein  $G$  and  $c$  as the common physical constants and  $M_{BH}$  as a BH mass), an outer radius of  $400R_g$ , an emissivity of 4, and an inclination of 55.7 degrees. The rest energies of these lines correspond to ionized iron-L and K, respectively. However, Fabian et al. (2009) found the iron abundance to be almost 9 times of the solar value, which they associated with the possible influence of a dense nuclear star cluster in the vicinity of 1H 0707, which can lead to the formation of massive double white dwarfs that enriched the core with iron-rich supernova emissions (Shara & Hurley 2002).

In the present paper, we made an assumption that this shape of the ionized iron-K line in the 1H 0707 spectrum may be due to the outflowing wind, which, to a first approximation, can be described by an iron line with a *Laor* profile. The presence of outflowing gas from the nuclear environment of 1H 0707 is supported by recent near-infrared spectroscopy in the *zJHK* bands, which revealed the dominance of broadband lines with low ionization. Namely, extensive components in H I, Fe II and O I were found, shifted at a velocity of  $\sim 500$  km/s. At the same time, most lines have a blue-asymmetric profile, the velocity shift of which is  $\sim 826$  km/s. This feature is consistent with previous indications of escape gas in 1H 0707, observed in the X-ray and UV lines, and now found in the low ionization lines. Rodriguez-Ardila et al. (2024) argue that the wind can propagate far into the region of the narrow line due to the observation of a blue-shifted component in the forbidden [S III]  $\lambda 9531 \text{ \AA}$  line. Xu et al. (2021) revealed absorption edges in the fits of the 1H 0707 spectra, which can also be interpreted as an evidence of a clumpy, multi-temperature outflow around 1H 0707. Therefore, to describe the 1H 0707 spectra, we used the `tbabs*(bmc+N×Laor)`. The *Laor* model parameters are the line energy,  $E_L$ , the emissivity index, a dimensionless inner disk radius,  $r_{in} = R_{in}/R_g$ , inclination,  $i$ , and the normalization of the line,  $N_L$  (in units of photons  $\text{cm}^{-2} \text{ s}^{-1}$ ).

For the *Laor* component we fixed the outer disk radius to the default value of  $400 R_g$  and vary all other parameters. We also fixed the emissivity index to 3. The inclination is constrained to a

value  $i \sim 50^\circ$ . As a result, in our spectral data analysis for all three sources we use a model which consists a sum of a Comptonization component (*BMC*) and *Gaussian (Laor)* line component for NGC 1566 and NGC 7679 (1H 0707). Let us recall that the *BMC* spectral component has the following parameters: the seed photon temperature,  $T_s$ , the energy index of the Comptonization spectrum  $\alpha$  ( $= \Gamma - 1$ ), a Comptonization fraction  $f$  [ $f = A/(1 + A)$ ], which is the relative weight of the Comptonization component and normalization of the seed photon spectrum,  $N_{com}$ . When the parameter  $\log(A) \Rightarrow \gg 1$  we fix  $\log(A) = 2$  because the Comptonized illumination fraction  $f = A/(1 + A) \rightarrow 1$  and variation of  $A$  does not improve the fit quality any more.

### 3.3.2. NGC 1566 Spectra

Spectral analysis of the NGC 1566 observations by *Suzaku* and *Swift* indicates that the source spectra can be reproduced by a model with an absorbed Comptonization component, the XSPEC *BMC* model<sup>13</sup> with the adding *Gaussian* iron line component. In Figures 12 and 13 we present examples of X-ray spectra of NGC 1566 indicating the spectral components in the range 0.3–10 keV and their evolution.

In the LHS, represented by the *Swift* observation (ID=00014916001), the spectrum of NGC 1566 is dominated by the hard emission component (Fig. 12, panel *a*), which is well reproduced by the Comptonization model with parameters:  $\Gamma=1.40\pm0.02$  and  $T_s=110\pm12$  eV (reduced  $\chi^2=0.95$  for 563 d.o.f). With better energy resolution in the LHS state, the spectrum of NGC 1566 with the *Suzaku* observation is also well described by the Comptonization component, but with an addition of a noticeable emission feature in the energy range  $\sim 6.4\text{--}7.0$  keV associated with neutral, H-like and He-like  $K_\alpha$  Fe lines (panel *b*, ID=707002010). The best-fit model parameters are  $\Gamma=1.77\pm0.04$ ,  $T_s=130\pm1$  eV and  $E_{line} = 6.36\pm0.04$  keV (reduced  $\chi^2=0.95$  for 563 d.o.f). In the *intermediate* state of NGC 1566 (ID=00014923002, panel *c*) the best-fit model parameters are  $\Gamma=2.01\pm0.04$  and  $T_s=118\pm5$  eV (reduced  $\chi^2=0.95$  for 86 d.o.f). In the panel *d* we present again the IS spectrum (ID=00035880003) in the HSS, for which the best-fit model parameters are  $\Gamma=2.1\pm0.1$ ,  $T_s=90\pm10$  eV (reduced  $\chi^2=0.99$  for 86 d.o.f). The data are presented by black crosses and the best-fit spectral model *tbabs\*(BMC+Gauss)* by red line. Bottom:  $\Delta\chi$  vs photon energy in keV (see more details in Table 4). In the bottom panels we present  $\Delta\chi$  versus photon energy in keV.

We clearly see that the change in spectral state from LHS to HSS in NGC 1566 is accompanied by a slight change in the seed photon temperature  $T_s$  between 90 and 130 eV and an increase in the  $\Gamma$  index from 1.1 to 2.1 (Fig. 14). In details, a number of X-ray spectral transitions of

---

<sup>13</sup><https://heasarc.gsfc.nasa.gov/xanadu/xspec/manual/Models.html>

NGC 1566 have been detected by *Swift* during 2007–2023. We have searched for common spectral and timing features that can be revealed during these spectral transition events. The X-ray light curve of NGC 1566 shows complex behavior in a wide range of timescales: from hours to years (e.g., Oknyansky et al. (2020, 2019)). Here we discuss the source variability on the timescales of hours. In Figure 6 we demonstrate the model parameter evolution for all analyzed outburst spectral transitions. As one can see from the *HR* panel (second from the top), all outbursts of NGC 1566 are characterized by a significant increase of the soft component (*HR1*, blue points). Some events also demonstrate an increase of hard component (*HR2*, pink points) in the decay outburst phase (see particular events at MJD 57,000 and 58,400–59,000).

We paid special attention to the flaring events of 2018 – 2019 (see Fig. 6). Following the terminology of the astronomical community, which previously discussed the changing-look in NGC 1566, we have identified four events *F1*, *F2*, *F3* and *F4* that occurred after the main flare of 2018 (it was not observed using *Swift*), indicated in Fig. 6 with using the pink arrows on top of the figure. Event *F1* occurred in December 2018 (Grupe et al. 2018), event *F2* occurred at the end of May 2019 (Grupe et al. 2019), event *F3* occurred in August 2019 (Oknyansky et al. 2020) and event *F4* in May 2020 (Jana et al. 2021).

The 2018 outburst itself began in March 2018 (58,200 MJD) according to the V-band ASSAS-SN and *Master* data (Oknyansky et al. 2019) data. *Swift*/XRT detected this outburst just a few months later, in June 24, 2018 (MJD 58,293.7), when the X-ray intensity increased to 30 times its quiescent state (see Figure 6). For this outburst with a good peak-decay coverage, the enhancement of the soft component (pink points in second panel from the top) during the decay phase (Fig. 6, MJD 58,452 – 58,749) correlates with the disappearance of broad lines and [Fe X]  $\lambda$  6374 Å to 58,561 in optical spectrum of NGC 1566 (Oknyansky et al. 2020), which may be due to an increase in the illumination of the accretion disk by soft X-rays. We can also suggest that the NGC 1566 spectral state evolution can be traced by the illumination fraction  $f$ . In fact, the parameter  $f$  increased greatly during these days ( $0.7 < f < 1$ ). The photon index  $\Gamma$  is well traced by soft X-ray flux (compare the bottom and two upper panels of Figure 6). In addition, this may be related to the moderate mass accretion rate regime. In fact, the BMC Normalization parameter ( $N_{com}$ ) and photon index ( $\Gamma$ ) for these dates are some lower (MJD 58,452–58,749) than for events at the peak of the 2018 outburst (MJD 58,293).

### 3.3.3. 1H 0707–495 Spectra

Spectral analysis of 1H 0707 observations by *Suzaku*, *ASCA*, *Swift* and *RXTE* indicates that source spectra can be reproduced by a model with a Comptonization component, the XSPEC *BMC* model. In Figures 13 and 15 we present examples of X-ray spectra of 1H 0707 indicating the



spectral components in the range 0.3–10 keV and their evolution. The BMC model provides a description of the X-ray emission from the source, which is processed by the accretion disk and/or the surrounding wind environment, with the disk producing the observed  $K_\alpha$  iron fluorescence lines and hump in the continuum. It is clearly seen that the energy range  $\sim 6.4\text{--}7.0$  keV is also modified by other lines associated with neutral, H-like and He-like  $K_\alpha$  Fe lines. We found a number of positive excesses in the spectrum and added a number of additional lines to better describe the spectrum. Using this approach, we found lines at energies of 6.4, 6.8, 2.9, 1.02, 0.85, 0.65 and 0.5 keV, which are easily associated with Fe I–XXII, Fe XXV/Fe XXVI  $K_\alpha$ , lines S XVI, Ne X, Fe XVII, O III and N XVII, respectively.

On panel (a) of Figure 15 we demonstrate the best-fit *Suzaku* spectrum of 1H 0707 which is a typical for the LHS using our model for observation ID=00091623 carried out on 3–6 December, 2005. The best-fit model parameters are  $\Gamma=1.79\pm 0.13$ ,  $T_s=121\pm 4$  eV and  $E_{line}=0.83\pm 0.02$  keV (reduced  $\chi^2=1.00$  for 802 d.o.f). In panels (b) and (c) of this figure, we have presented the source spectra for the IS using the Swift observation (ID=00091623002 and observation ASCA ID=73043000). The best-fit model parameters for ID=00091623002 are  $\Gamma=2.00\pm 0.10$ ,  $T_s=120\pm 5$  eV and  $E_{line}=0.85\pm 0.08$  keV (reduced  $\chi^2=1.06$  for 189 d.o.f). The best-fit model parameters for ID=73043000 are  $\Gamma=2.03\pm 0.09$ ,  $T_s=107\pm 4$  eV and  $E_{line}=0.83\pm 0.09$  keV (reduced  $\chi^2=1.01$  for 86 d.o.f).

Finally, in the panel (d) we showed the spectrum of 1H 0707 in the HSS using observation Swift ID=00080720048, for which the best-fit model parameters are  $\Gamma=2.9\pm 0.1$ ,  $T_s=230\pm 10$  eV and  $E_{line}=0.86\pm 0.09$  keV (reduced  $\chi^2=0.97$  for 158 d.o.f). The data are presented by black crosses and the best-fit spectral model  $tbabs*(BMC+N*Laor)$  by red line. Bottom:  $\Delta\chi$  vs photon energy in keV (see more details in Table 4). Thus, we clearly see that the change in spectral state from the LHS to the HSS in 1H 0707 is accompanied by a slight change of the seed photon temperature  $T_s$  between 100 and 230 eV and an increase in the  $\Gamma$  index from 1.1 to 2.9 (Fig. 16). For the LHS, we combine the *Suzaku* and *RXTE* observations (see Table 2) to demonstrate that the source spectrum varies over a wide energy range from 0.3 to 200 keV (Fig. 13). In this case, the dominance of the hard (10–100 keV) emission of 1H 0707 with a slight excess of the soft component at 0.3–2 keV is obvious.

### 3.3.4. NGC 7679 Spectra

In Figure 17 we show three representative spectra of NGC 7679 for the LHS, HIMs and IS. We again simulate the spectra using the plasma Comptonization process (BMC) with an addition of a *Gaussian* iron line component. The best-fit modeling of the NGC 7679 spectrum in the LHS is presented on the left panel using from *BeppoSAX* data (ID=40631001) in units of  $E * F(E)$ .

The broadband spectrum [0.3–200 keV] demonstrates a hard tail and has the best-fit parameters:  $\Gamma=1.60\pm 0.02$ ,  $T_s=350\pm 60$  eV and  $E_{line}=6.4\pm 0.5$  keV (reduced  $\chi^2=1.04$  for 82 d.o.f). In central panel of this Figure, we presented the source spectra which are typical for *hard intermediate state* (HIMS) using ASCA observation (ID=66019000). The best-fit parameters are  $\Gamma=1.62\pm 0.02$ ,  $T_s=150\pm 70$  eV and  $E_{line}=6.5\pm 0.1$  keV (reduced  $\chi^2=1.09$  for 145 d.o.f). Finally, on the right panel we present the IS spectrum (ID=00088108002) of NGC 7679 observed by *Swift*/XRT. The best-fit model parameters are  $\Gamma=1.93\pm 0.07$  and  $T_s=226\pm 9$  eV (reduced  $\chi^2=0.97$  for 194 d.o.f). The data are denoted by crosses, while *red* and *pink* lines stand for the *BMC* and *Gaussian* components, respectively. Bottom panels demonstrate  $\Delta\chi$  versus photon energy in keV.

### 3.3.5. Mrk 3 Spectra

In Figure 18 we show four representative spectra of Mrk 3 for the LHS and IS states. We simulate these spectra using the BMC model with an addition of a *Gaussian* iron line component. The best-fit model of the Mrk 3 spectrum of the LHS is presented in panel (a) using from ASCA data (ID=70002000) in units of  $E * F(E)$ . The best-fit parameters are  $\Gamma=1.102\pm 0.02$ ,  $T_s=180\pm 10$  eV and  $E_{line}=6.41\pm 0.09$  keV (reduced  $\chi^2=1.05$  for 52 d.o.f). In panels (b – d) of the Figure, we present the source spectra which are typical for the IS using *Suzaku* (ID=100040010, panel b), *RXTE* (ID=20330-01-09-00, panel c) and *BeppoSAX* (ID=50132002, panel d) observations. The best-fit parameters for this *Suzaku* observation are  $\Gamma=1.10\pm 0.02$ ,  $T_s=100\pm 10$  eV and  $E_{line}=6.41\pm 0.05$  keV (reduced  $\chi^2=0.94$  for 629 d.o.f). The best-fit parameters for the *RXTE* observation are  $\Gamma=1.11\pm 0.01$ ,  $T_s=300\pm 20$  eV and  $E_{line}=6.38\pm 0.08$  keV (reduced  $\chi^2=0.86$  for 47 d.o.f). The best-fit model parameters for *BeppoSAX* spectrum are  $\Gamma=1.55\pm 0.04$ ,  $T_s=230\pm 30$  eV and  $E_{line}=6.40\pm 0.08$  keV (reduced  $\chi^2=0.90$  for 84 d.o.f). The data are denoted by crosses, while *red* and *pink* lines stand for the *BMC* and *Gaussian* components, respectively. Bottom panels demonstrate  $\Delta\chi$  versus photon energy in keV.

## 3.4. Comparative analysis of X-ray patterns of CL-, Sy1- and Sy2-AGNs during transient events

Spectral analysis of the X-ray spectra for CL-, Sy1- and Sy2-AGN showed that the emission of all these AGNs can be reproduced by the absorption model and the Comptonization one applying in addition to linear characteristics. However, the Comptonization hump parameters and emission features are very different for Sy1 and Sy2. CL-AGN is a combination of Sy1 and Sy2 properties depending on the Eddington-normed X-ray luminosity level of CL-AGN. The Comptonization hump, characterized primarily by the  $\Gamma$  index, shows different shapes and energy positions in the

spectrum. To make this more convincing, we have added the results found in the literature [e.g. Weng et al. (2020), Hernandez-Garcia et al. (2015)]. As a result, for Sy1  $\Gamma$  varies in moderate limits (from 1.1 to 2.9), while for Sy2  $\Gamma$  varies in a wider range: from 1.6 to 2.9. For CL  $\Gamma$  varies in rather narrow limits: from 1.3 to 1.9. Taking into account the different masses of the objects (see Fig. 19), we compare them and their X-ray luminosities normalized to the Eddington luminosity  $L_x/L_{Edd}$  for 1H 0707, NGC 1566, NGC 7679 and Mrk 3 (all indicated by black arrows in Fig. 19). In this Figure we can see the different positions of Sy1 (blue squares), Sy2 (red stars) and CL-AGN (marked by black background circles) on the  $L_x/L_{Edd}$  diagram for NGC 1566 (in the purple box), 1H 0707 (in the pink box) and NGC 7679 and Mrk3 (in the green box). There the grey arrow shows the critical value of  $3.5 \times 10^{-4} L_x/L_{Edd}$  which separates Sy1 from Sy2. In addition to this obvious difference in the relative X-ray luminosities of Sy1 and Sy2, their difference in photon index is immediately visible. Sy2 shows a wide  $\Gamma$  range, while Sy1 is somewhat smaller (tending to high  $\Gamma$ ) and CL-AGN is very narrow. At the same time, an interesting property of CL-AGN is revealed in contrast. Namely, with a small change in  $\Gamma$  they reach the relative X-ray luminosities of both Sy1 and Sy2. Apparently, CL-AGN is capable of making such a jump in  $L_x/L_{Edd}$  that at low relative luminosities it looks like Sy2 (in the green box region), and at relatively high luminosities (in the pink box region).

It is worth noting that Sy1 and Sy2 AGNs are not differentiated by a BH mass ( $2 \times 10^5 - 5 \times 10^8$ ) in our AGN sample (Fig. 20), but show different tracks on the  $\Gamma - M_{BH}$  diagram: Sy1 (blue squares) tend to  $\Gamma \sim 1.5 - 2$ , while Sy2 (red stars) have a larger spread in  $\Gamma$  (1.6–2.8).

It is worth noting that the emission from NGC 1566 and NGC 7679 is strongly subject to reprocessing in the inner parts of the disk, the Compton cloud, for which  $0.3 < f < 1$  and thus, only some fraction of disk emission component ( $1 - f$ ) is directly seen by the Earth observer. While a degree of irradiation of 1H 0707 remains low all the time ( $0.05 < f < 0.08$ ). It is interesting that the temperature of the disk seed photons,  $kT_s$ , is almost the same for all three objects of different subclasses and varies slightly from 100 to 300 eV (see Table 4).

We also found that during the transition from Sy2 to Sy1, the NGC 1566 spectrum shows an increase in the soft excess (Fig. 13), accompanied by a decrease in the illumination degree ( $0.1 < f < 0.5$ ), which can be associated with the entry into the Sy1 state during the outburst (Fig. 6), so thereby blurring the line between the two subclasses. Our results strongly suggest that the large diversity in the behavior observed among CL, Sy1 and Sy2 AGNs with different Eddington-normed X-ray luminosities can be explained by changes in a single variable parameter, namely the mass accretion rate, without any need for additional differences in Sy AGN parameters or its inclination.

### 3.5. A BH mass estimate

We used a scaling technique to estimate a BH mass  $M_{BH}$ , previously developed specifically for BH weighing Titarchuk et al. (2024); Titarchuk and Seifina (2023); Titarchuk et al. (2023); Seifina et al. (2018a,b, 2017). We used the  $\Gamma - N$  correlation to estimate the mass of BHs (for details see Shaposhnikov and Titarchuk (2009), ST09). This method ultimately (i) identifies a pair of BHs for which  $\Gamma$  correlates with an increasing normalization of  $N$  (which is proportional to a mass accretion rate  $\dot{M}$  and a BH mass  $M$ , see ST09, Eq. (7)) and for which the saturation levels  $\Gamma_{sat}$ , are the same and (ii) calculates the scaling factor  $s_N$ , which allows us to determine a black hole mass of the target object. It should also be emphasized that to estimate a BH mass using the following equation for the scale factor, the ratio of the distances to the *target* and *reference* sources is necessary:

$$s_N = \frac{N_r}{N_t} = \frac{m_r d_t^2}{m_t d_r^2} f_G, \quad (3)$$

where  $N_r$  and  $N_t$  are normalizations of the spectra,  $m_t = M_t/M_\odot$  and  $m_r = M_r/M_\odot$  are the dimensionless BH masses with respect to a solar mass, and  $d_t$  and  $d_r$  are distances to the *target* and *reference* sources, correspondingly. A geometrical factor,  $f_G = \cos i_r / \cos i_t$ , where  $i_r$  and  $i_t$  are the disk inclinations for the *reference* and *target* sources, respectively (see ST09, Eq. (7)).

#### 3.5.1. A BH mass estimate in NGC 1566

For appropriate scaling, we need to select X-ray sources (reference sources), which also show the effect of the index saturation, namely at the same  $\Gamma$  level as in NGC 15660707–495 (target source). For reference sources, a BH mass, inclination, and distance must be well known. We found that NGC 4051, GX 339–4, GRO J1655–40, Cyg X–1 and 4U 1543–47 can be used as the reference sources because these sources met all aforementioned requirements to estimate a BH mass of the target sources NGC 1566 and NGC 7679 (see items (i) and (ii) above).

In Figure 14 we demonstrate how the photon index  $\Gamma$  evolves with normalization  $N$  (proportional to the mass accretion rate  $\dot{M}$ ) in NGC 1566 (*target* source) and NGC 4051, GX 339–4, GRO J1655–40, Cyg X–1 and 4U 1543–47 (*reference* sources), where  $N$  is presented in units of  $L_{39}/d_{10}^2$  ( $L_{39}$  is the source luminosity in units of  $10^{39}$  erg/s and  $d_{10}$  is the distance to the source in units of 10 kpc). As we can see from this Figure that these sources have almost the same index saturation level  $\Gamma$ . We estimated a BH mass for NGC 1655 using the scaling approach (see e.g., ST09). In Figure 14 we illustrate how the scaling method works shifting one correlation versus another. From these correlations we could estimate  $N_t$ ,  $N_r$  for NGC 1566 and for the reference sources (see Table 6). A value of  $N_t = 1.04 \times 10^{-4}$ ,  $N_r$  in units of  $L_{39}/d_{10}^2$  is determined in the beginning of the  $\Gamma$ -saturation part (see Fig. 6, ST07, ST09, Titarchuk et al. (2014); Titarchuk and

Seifina (2016a,b, 2009)).

A value of  $f_G = \cos i_r / \cos i_t$  for the *target* and *reference* sources can be obtained using trial inclination for NGC 1566  $i_t = 60^\circ$  and for  $i_r$  (see Table 6). As a result of the estimated target mass  $m_t$  (in NGC 1566), we find that

$$m_t = f_G \frac{m_r d_t^2}{s_N d_r^2}, \quad (4)$$

where we used values of  $d_t = 21.3$  Mpc (see Table 1).

Applying Eq.(4), we can estimate  $m_t$  (see Table 6) and we find that the secondary BH mass in NGC 1566 is about  $1.9 \times (1 \pm 0.20) \times 10^5 M_\odot$ . To obtain this estimate with appropriate error bars, we need to consider error bars for  $m_r$  and  $d_r$  assuming, in the first approximation, errors for  $m_r$  and  $d_r$  only. We rewrote Eq. (4) as

$$m_t(1 + \Delta m_t/m_t) = f_G \frac{m_r d_t^2}{s_N d_r^2} (1 + \Delta m_r/m_r)(1 + 2\Delta d_r/d_r). \quad (5)$$

Thus, we obtained errors for the  $m_t$  determination (see Table 6, second column for the *target* source), such that

$$\Delta m_t/m_t \sim \Delta m_r/m_r + 2\Delta d_r/d_r. \quad (6)$$

As a result, we find that  $M_{1566} \sim 1.9 \times 10^5 M_\odot$  ( $M_{1566} = M_t$ ) assuming  $d_{1566} = 21.3$  Mpc for NGC 1566. We present all these results in Table 6. In order to calculate the dispersion  $\mathcal{D}$  of the arithmetic mean  $\bar{m}_t$  for a BH mass estimate using different reference sources  $\mathcal{D}$  (see Table 6), one should keep in mind that

$$\mathcal{D}(\bar{m}_t) = D/n, \quad (7)$$

where  $D$  is the dispersion of  $m_r$  using each of the reference sources and  $n = 5$  is a number of the reference sources. As a result we determined that the mean deviation of the arithmetic mean

$$\sigma(\bar{m}_t) = \sigma / \sqrt{n} \sim 0.20 \quad (8)$$

and finally we came to the following conclusion (see also Table 6):

$$\bar{m}_t \sim 1.9 \times (1 \pm 0.20) \times 10^5 M_\odot. \quad (9)$$

### 3.5.2. A BH mass estimate in NGC 7679

Figure 14 we illustrate how the scaling method works shifting one correlation versus another. From these correlations we could estimate  $N_t$ ,  $N_r$  for NGC 7679 and for the reference sources (see Table 6). A value of  $N_t = 5 \times 10^{-4}$ ,  $N_r$  in units of  $L_{39}/d_{10}^2$  is determined in the beginning of the  $\Gamma$ -saturation part (see Fig. 14).

In a similar way and using the same reference sources as for NGC 1566, we determined a BH mass in NGC 7679 (see also Table 6):

$$\bar{m}_t \sim 8.4 \times (1 \pm 0.20) \times 10^6 \text{ M}_\odot, \quad (10)$$

where we used values of  $d_t = 57.28$  Mpc and source inclination  $i_t = 30^\circ$  (see Table 1).

### 3.5.3. A BH mass estimate in Mrk 3

In Figure 14 we illustrate how the scaling method works for Mrk 3. In this case, we used five reference sources NGC 4051, GX 339–4, GRO J1655–40, Cyg X–1 and 4U 1543–47, as well as for NGC 1566 and NGC 7679. From these correlations we were able to estimate  $N_t$ ,  $N_r$  for Mrk 3 and for the reference sources (see Table 6). The value  $N_t = 0.1$ ,  $N_r$  in units of  $L_{39}/d_{10}^2$  is determined at the beginning of the  $\Gamma$ -saturation part (see Fig. 14).

In a similar manner to Sects. 3.5.1 and 3.5.2 as well as using the same reference sources as for NGC 1566 and 7679, we determined the mass of the BH in Mrk 3 (see also Table 6):

$$\bar{m}_t \sim 2.2 \times (1 \pm 0.20) \times 10^8 \text{ M}_\odot, \quad (11)$$

where we used values of  $d_t = 63.2$  Mpc and source inclination  $i_t = 50^\circ$  (see Table 1).

### 3.5.4. A BH mass estimate in 1H 0707–495

We found that SDSS J0752, OJ 287, M101 ULX–1 and ESO 243 HLX–1 can be used as the reference sources because these sources met all aforementioned requirements to estimate a BH mass of the target source 1H 0707.

In Figure 16 we demonstrate how the photon index  $\Gamma$  evolves with normalization  $N$  in 1H 0707 (*target* source) and SDSS J0752, OJ 287, M101 ULX–1 and ESO 243 HLX–1 (*reference* sources), where  $N$  is presented in units of  $L_{39}/d_{10}^2$ . As we can see from this Figure that these sources have almost the same index saturation level  $\Gamma$  about 2.8–2.9. We estimated a BH mass for 1H 0707–495 using the scaling approach (see e.g., ST09). In Figure 16 we illustrate how the scaling method works shifting one correlation versus another. From these correlations we can estimate  $N_t$ ,  $N_r$  for 1H 0707 using the reference sources (see Table 5). A value of  $N_t = 3.5 \times 10^{-3}$ ,  $N_r$  in units of  $L_{39}/d_{10}^2$  is determined in the beginning of the  $\Gamma$ -saturation part (see Fig. 5).

To determine the distance to 1H 0707-495 we used the formula (for  $z < 1$ )

$$d_{0707} = z_{0707}c/H_0 \simeq 160 \text{ Mpc}, \quad (12)$$

where the redshift  $z_{0707} = 0.004$  for 1H 0707,  $H_0 = 70.8 \pm 1.6 \text{ km s}^{-1} \text{ Mpc}^{-1}$  is the Hubble constant and  $c = 3 \times 10^5 \text{ km/c}$  is the speed of light. This distance  $d_{0707}$  agrees with the luminosity distance estimate using Ned Wright’s Javascript Cosmology Calculator<sup>14</sup>  $d_{1H0707}^{NW} \sim 170 \text{ Mpc}$  Wright (2006).

A value of  $f_G$  for the *target* and *reference* sources can be obtained using the trial inclination for 1H 0707  $i_t = 55^\circ$  and for  $i_r$  (see Table 5).

We estimated the target BH mass,  $m_t$  (1H 0707) (see also Table 5):

$$\bar{m}_t \sim 6.8 \times (1 \pm 0.27) \times 10^7 M_\odot, \quad (13)$$

where we used values of  $d_t = 160 \text{ Mpc}$ . Here we also calculated the dispersion  $\mathcal{D}$  of the arithmetic mean  $\bar{m}_t$  for a BH mass using different reference sources  $\mathcal{D}$  (see Table 5)

$$\sigma(\bar{m}_t) = \sigma / \sqrt{n} \sim 0.27, \quad (14)$$

wherein  $n = 4$ .

## 4. Discussion

We argued that the emission of all considered AGNs (NGC 1566, 1H 0707, NGC 7679 and Mrk 3) shows variability and has a flaring nature, presumably due to a change in the rate of accretion of matter in the central regions of each AGN. We found that the X-ray spectra for these CL, Sy1 and Sy2 AGNs can contribute to our understanding of the differences between these AGN subclasses. Their differences immediately follow from different patterns of variability and different luminosity levels of the sources. However, we found differences and similarities between them. Emission from NGC 1566 during changing-look can be associated with different combinations of hard and soft components of the spectra depending on the level of relative luminosity ( $L_x/L_{Edd}$ ) of NGC 1566. This source uniquely combines the properties of Sy1 and the properties of Sy2: at high relative luminosities NGC 1566 demonstrates behavior typical for Sy1, and at low relative luminosities we observed a transition of NGC 1566 from Sy1 behavior to Sy2 one.

Furthermore, as a result of the comparative analysis, we found spectral distinctive features between Sy1 and Sy2, which are easy to detect. In fact, the evaluation of two observable quantities (the photon index  $\Gamma$  and relative X-ray luminosity  $L_x/L_{Edd}$  of AGNs shows a strong difference for Sy1 and Sy2. AGNs that fall in both regions of Sy1 and Sy2 in terms of  $L_x/L_{Edd}$  are candidates for CL-AGNs (see Fig. 19).

---

<sup>14</sup><https://www.astro.ucla.edu/wright/CosmoCalc.html>

An intriguing question is what would be the mechanism for such abrupt switching on or off of CL AGN power generation. It was studied by Katebi et al. (2019); Lyuty et al. (1984); Penston & Perez (1984); Runnoe et al. (2016); Lightman & Eardley (2007); Liu et al. (2020); MacLeod et al. (2019); Parker et al. (2019); Ruan et al. (2019); Sniegowska et al. (2021); Oknyansky et al. (2020). Several different possibilities have been considered: variable dimming, disk accretion flares, tidal disruption events, and a supernova event (see, for example, Oknyansky20). We found that a BH mass in CL-AGN NGC 1566, determined by scanning X-ray properties and the detected saturation of the index in NGC 1566 ( $\alpha_{1566} \sim 1.7$ ), turned out to be one or two orders of magnitude lower than a BH mass, determined from optical observations. This may indicate a possible duality of the SMBH at the level of the center of NGC 1566. This fact may be one of the reasons for a rapid change in the accretion rate, which leads to a change observed in the NGC 1566 galaxy.

During the outbursts, we found the index saturation in all three sources, which is consistent with the spectral signature of the presence of a BH in these sources (TC09). Based on the saturation effect, we estimated a BH mass in each source. It should be noted that a BH mass in NGC 1566 indicates a possible nature of the variability of NGC 1566 associated with the presence of a second, more massive BH in the center of NGC 1566. Interestingly, a BH mass of the BH in 1H 0707 is slightly larger than those based on reverberation delays Zhou & Wang (2005); Kara et al. (2013); Done & Jin (2016), which may indicate a presence of an additional soft X-ray source, for example, associated with enhanced star formation Sani et al. (2010); Zoghbi et al. (2010). A BH mass in NGC 7679 is consistent with the estimates by other authors available in the literature Woo & Urry (2002); Elagali et al. (2019); Fabian et al. (2009).

In addition, we compared our results with those of other authors. For example, Jana et al. (2021) performed an analysis of the X-ray emission from NGC 1566 during its June 2018 outburst observed by *Swift*. They analyzed quasi-simultaneous observations of this source obtained with *NuSTAR* and *XMM-Newton* using models (power-law and NthCOMP) different from ours (BMC+Gauss).

Moreover, our results are consistent with their conclusions, according to which a strong excess of soft X-ray emission was detected in the spectra during the outburst. We also found a soft excess, clearly visible in the central panel of Fig. 13 (red spectrum) and panel *d* in Fig. 12. However, our model makes it possible to compensate it increasing a fraction of disk soft photons, caused by an enlargement of the irradiation parameter  $f$ . Indeed, soft excess emission occurs in the thermal Comptonization region of the inner accretion disk (Compton cloud, see Titarchuk and Seifina (2023); Titarchuk et al. (2023); Titarchuk and Seifina (2021); Titarchuk et al. (2020); Titarchuk and Seifina (2017, 2016a,b); Titarchuk et al. (2014, 2010). Jana et al. (2021) found that an increase of the mass accretion rate is responsible for a sudden growth of source luminosity. They based on the  $q$ -shaped shape of the hardness-intensity diagram that is commonly found in



flaring BH X-ray binaries. We also came to the conclusion that the main driver of a sharp flare is due to a sharp increase of the mass accretion rate. We explain this behavior using normalization parameter  $N_{com}$  of the Comptonization radiation and its typical growth with a flare up to the peak flare saturation (Titarchuk and Seifina 2009).

It was worthwhile to emphasize that Jana et al. (2021) found a constancy (or weak variability) of the index during the *NuSTAR* and *XMM-Newton* observations of NGC 1566 at the level of  $\Gamma = 1.7 - 1.9$ . This differs from our results for the joint *Swift*, *NuSTAR* and *XMM-Newton* data analysis, when the  $\Gamma$  index varies widely from 1 to 2. It is possible that such a difference in the  $\Gamma$  behavior, discovered by us, is related with the use of different spectral models. However, this difference is due to the specific distribution of the observational time for NGC 1566. These *NuSTAR* observations were rare and fell precisely on the peaks of the primary outburst and the peaks of the secondary outbursts or close to them (see Fig. 6). They fall exactly on the saturation region of the  $\Gamma - N_{BMC}$  plot (top left panel in Fig. 21), when the index is maintained at  $\Gamma = 2$  for high source luminosities (Figs. 14, 16 and 21).

The use of different models for modeling AGN spectra sheds light on different features of AGNs. In this case, the use of special models such as agnsed (Kubota & Done 2018) and dual-coronal (Petrucci et al. 2013), which take into account the geometry of AGNs with different zones (outer standard disk, inner warm Comptonizing region and hot corona), determine well the thermal component of Comptonization to reveal the soft X-ray excess in the spectra of AGNs in the LHS state. Petrucci et al. (2013) used mainly the thermal Comptonization component to describe the soft X-ray excess in the AGN spectra in the LHS. Their Figure 10 correctly represents the geometry of the accretion flow in the inner region of the galaxy Mrk 509. However, Petrucci et al. (2013) do not find any spectral evolution, for example, in the source Mrk 509. In contrast, the photon index in our BMC or COMPTB models has an upper limit of 3 with all the signs of photon index saturation. This is clearly confirmed by our spectral numerical and analytical calculations of the convergent flow spectra (see Titarchuk & Zannias (1998); Laurent & Titarchuk (1999)).

Interestingly, Jana et al. (2021) discusses a scenario in which the central nucleus of NGC 1566 could be a merging SMBH. We also come to a similar conclusion, but we based on an estimate a BH mass at the center of NGC 1566 applying X-ray data. Since our “X-ray BH mass estimate” turned out to be two orders of magnitude lower than the optical one, we can assume a presence of a binary system of SMBHs of different masses in the center of NGC 1566. Similar situations have been observed before (Seifina et al. 2023; Titarchuk et al. 2023, 2024). In these cases, a lower BH mass (secondary BH), being more mobile, orbiting around a more massive BH (primary BH), causes X-ray outbursts as it passes through the disk around the primary BH. The X-ray method for a BH mass estimate determines a BH mass only of the secondary BH. It is clear that the primary BH does not appear in the X-ray range, although it does appear in the optical range and here its

mass dominates the contribution of the secondary BH, especially when one estimates a BH mass using stellar kinematics and dynamics methods (Woo & Urry 2002; Elagali et al. 2019).

## 5. Conclusions

We present our analysis of the spectral properties observed in X-rays from the NGC 1566, 1H 0707–495, NGC 7679 and Mrk 3 during long-term transitions between the faint phase and the bright phase.

We analyze transition episodes for these sources observed by *Swift*, *BeppoSAX*, *Suzaku*, *ASCA*, *NuSTAR*, *XMM-Newton* and *RXTE*. We show that the X-ray spectra for CL, Sy1 and Sy2 during all spectral states can be well fitted by a composition of the Comptonization and *Gaussian/Laor* components. We argued that these changes in the X-ray properties of NGC 1566 are characterized by a different combination of Sy1 and Sy2 properties. At high luminosities NGC 1566 exhibits a behavior which is typical for Sy1, and at low luminosities we observed a transition of NGC 1566 from the Sy1 behavior to the Sy2 one.

We discovered the saturation of the photon index for these four AGNs during outbursts ( $\Gamma_{1566} \sim 2.1$ ,  $\Gamma_{0707} \sim 3$ ,  $\Gamma_{7679} = 1.9$  and  $\Gamma_{mrk3} = 1.9$ ) and estimated the masses of the SMBHs in the centers of these AGNs:  $M_{0707} \sim (6.8 \pm 0.27) \times 10^7 M_{\odot}$ ,  $M_{7679} \sim (8.4 \pm 0.2) \times 10^6 M_{\odot}$ ,  $M_{mrk3} \sim (2.2 \pm 0.2) \times 10^8 M_{\odot}$  and  $M_{1566} \sim (1.9 \pm 0.2) \times 10^5 M_{\odot}$  by the scaling method. Notably, the X-ray scaled BH mass in CL-AGN NGC 1566 is one to two orders of magnitude lower than the BH mass determined from optical observations, indicating a possible duality of the SMBH at the center of NGC 1566. This may be one of the reasons for a rapid change in the accretion rate, which leads to a changing look observed in the NGC 1566 galaxy.

We also find that when CL-AGN transits from Sy2 to Sy1, the spectrum of NGC 1566 shows an increase of the soft excess accompanied by a decrease in the luminosity fraction ( $0.1 < f < 0.5$ ), which is consistent with a typical behavior of BH sources during X-ray outburst decay.

Our results strongly suggest that the large diversity in the behavior observed among CL, Sy1, and Sy2 AGNs with different X-ray luminosities can be explained by changes of a single variable parameter, such as the ratio of the AGN’s X-ray luminosity to its Eddington mass accretion rate, without any need for additional differences in Sy AGN parameters, such as its inclination, thereby blurring the distinction between the Sy1, Sy2 and CL-AGN subclasses.

### Acknowledgements

This research has made using the data and/or software provided by the High Energy Astrophysics Science Archive Research Center (HEASARC), which is a service of the Astrophysics Science Division at NASA/GSFC and the High Energy Astrophysics Division of the Smithsonian Astrophysical Observatory. We appreciate valuable remarks by Chris Schrader on the paper and thank Juliana Seifina for her assistance in preparing the figures. We acknowledge the interesting remarks and points of the referee. The *Swift* data is available to download through the UK Swift Data Science website <https://www.swift.ac.uk/archive>.

### REFERENCES

- Aguero, E. L., Diaz, R. J., & Bajaja, E. 2004, A&A, 414, 453
- Alonso-Herrero, A., Pereira-Santaella, M., Rieke, G. H. et al. 2013, ApJ, 765, 78
- Antonucci R., 1993, ARA&A, 31, 473
- Awaki, H., Koyama, K., Kunieda H., Tawara, Y., 1990, Nature, 346, 544
- Awaki, H., Koyama, K., Inoue, H., Halpern, J.P., 1991, PASJ, 43, 195
- Belloni, T., Homan, J., Casella, P., et al. 2005, A&A, 440, 207
- Bentz, M. C., Katz, S., 2015, PASP, 127, 67
- Bentz M. C., et al., 2009, ApJ, 705, 199
- Boella, G. et al. 1997, A&AS, 122, 327
- Boller, Th. et al. 2002 MNRAS, 329, L1
- Borozdin, Revnivtsev, Trudolyubov, Shrader, & Titarchuk, 1999, ApJ, 517, 367
- Botte V., Ciroi S., Rafanelli P., Di Mille F., 2004, AJ, 127, 3168
- Bradt, H. V., Rothschild, R. E. & Swank, J. H. 1993, A&AS, 97, 355
- Boorman, P. G., Gandhi, P., Baloković, M., 2018, MNRAS, 477, 3775
- Cappi M. et al. 1999, A&A, 344, 857
- Christopoulou, P. E., Holloway, A. J., Steffen, W. et al. 1997, MNRAS, 284, 385

- Cutri R. M., Mainzer A. K., Dyk S. D. V., Jiang N., 2018, *Astronomers Telegram*, 11913, 1
- Dai X., Stanek K. Z., Kochanek C. S., Shappee B. J., ASAS-SN Collaboration, 2018, *Astronomers Telegram*, 11893, 1
- da Silva, P., Steiner, J. E., & Menezes, R. B. 2017, *MNRAS*, 470, 3850
- Della Ceca, R., Pellegrini, S., Bassani, L. et al. 2001, *A&A*, 375, 781
- Denney, K. D., Watson, L. C., Peterson, B. M. et al., 2009, *ApJ*, 702, 1353
- de Vaucouleurs, G., 1973, *ApJ*, 181, 31
- de Vaucouleurs G., de Vaucouleurs A., Corwin Jr. H.G., et al., 1991, *Third Reference Catalogue of Bright Galaxies*, Springer Verlag, New York.
- de Vaucouleurs, G., & de Vaucouleurs, A. 1961, *MmRAS*, 68, 69
- Done, C. & Jin, C., 2016, *MNRAS* 460, 1716
- Done, C., Davis, S. W., Jin, et al. 2012, *MNRAS*, 420, 1848
- Ducci, L., Siebert, T., Diehl, R. et al., 2018, *Astronomers Telegram*, 11754, 1
- Dunn J. P., Crenshaw D. M., Kraemer S. B., Trippe M. L., 2008, *AJ*, 136, 1201
- Elagali, A., et al. 2019, *MNRAS*, 487, 2797
- Elvis M., et al., 1994, *ApJS*, 95, 1
- Evans, P. A., Beardmore, A. P., Page et al. 2009, *MNRAS*, 397, 1177
- Evans, P. A., Beardmore, A. P., Page, K. L. et al. 2007, *A&A*, 469, 3795
- Gu Q., Melnick J., Cid Fernandes R., Kunth D., Terlevich E., Terlevich R., 2006, *MNRAS*, 366, 480
- Georgantopoulos, I., Papadakis, I., Warwick, R. S. et al., 1999, *MNRAS*, 307, 815
- Farinelli, R. & Titarchuk, L., 2011, *A&A*, 525, 102
- Griffiths, R. G., Warwick, R. S., Georgantopoulos, I. et al., 1998, *MNRAS*, 298, 1159
- Greene, J., Baily, C. D., & Orosz, J. A. 2001, *ApJ*, 554, 1290
- Grupe, D., Mikula, R., Komossa, S. et al. 2018, *The Astronomer's Telegram*, 12314

- Grupe, D., Mikula, R., Komossa, S. et al. 2019, The Astronomer’s Telegram, 12826, 1
- Fabian A. C., Lohfink A., Kara E., Parker M. L., Vasudevan R., Reynolds C. S., 2015, MNRAS, 451, 4375
- Fabian, A. C., Zoghbi, A., Ross, R. R. et al. 2009, Nature, 459, Issue 7246, 540
- Fabian, A.C. et al. 2004 MNRAS, 353, 1071
- Frontera, F. et al. 1997, SPIE, 3114, 206
- Jana, A., Kumari, N., Nandi, P. et al. 2021, MNRAS, 507, 687
- Grupe D. et al., 2018b, Astronomers Telegram, 12314, 1
- Grupe D. et al., 2019, Astronomers Telegram, 12826, 1
- Haba, Y., Liebmann, A. C., Fukumura, K., 2008, Publ. Astron. Soc. Japan, 60, 1257
- Hancock, S.; Young, A. J.; Chainakun, P., 2023, MNRAS, 520, 180
- Hartmann D., Burton W. B., 1997, Cambridge University Press Heckman T. M., 2000, In “Gas & Galaxy Evolution” conference proceedings, astro-ph/0009075
- Hernandez-Garcia, L. et al. 2015, A&A, 579, A90
- Herrero, J., et al. 1995, A&A, 297, 556
- Hjellming, R. M., & Rupen, M. P. 1995, Nature, 375, 464
- Hynes, R. I., Steeghs, D., Casares, J., Charles, P. A., & O’Brien, K. 2004, ApJ, 609, 317
- Hu C., Wang J.-M., Ho L. C., Bai J.-M., Li Y.-R., Du P., Lu K.-X., 2016, ApJ, 832, 197
- Iwasawa, K., Yaqoob, T., Awaki, H., Ogasaka, Y., 1994, PASJ, 46, L167
- Leighly K. M., 1999, ApJS, 125, 297
- Kara E., Fabian A. C., Cackett E. M., Steiner J. F., Uttley P., Wilkins D. R., Zoghbi A., 2013a, MNRAS, 428, 2795
- Katebi, R., Chornock, R., Berger, E. et al. 2019, MNRAS, 487, 4057
- Kewley L. J., Heisler C. A., Dopita M. A., 2001, ApJS 132, 37
- Klein-Wolt, M., & van der Klis, M. 2008, ApJ, 675, 1407

- Koyama, K., Tsunemi, H., Dotani, T. et al. 2007, PASJ, 59, S23
- Kubota, A. & Done, Ch., 2018, MNRAS, 480, 1247
- Laurent, P., & Titarchuk, L. 1999, ApJ, 511, 289
- Lightman, A. P., & Eardley, D. M. 1974, ApJ, 187, L1
- Liu, Z., Liu, H.-Y., Cheng, H., Qiao, E., & Yuan, W. 2020, MNRAS, 492, 2335
- Lyutyj, V.M., Oknyanskij, V. L., & Chuvaev, K. K. 1984, Soviet Astronomy Letters, 10, 335
- MacLeod, C. L., Green, P. J., Anderson, S. F. et al. 2019, ApJ, 874, 8
- Matt G., Guainazzi M., Maiolino R., 2003, MNRAS, 342, 422
- Matt, G., Fabian, A. C., Guainazzi, M., 2000, MNRAS, 318, 173
- Mitsuda K. et al., 2007, PASJ, 59, S1
- Laor, A., 1991 ApJ, 376, 90
- Lobban, A. P., Reeves, J. N., Miller, L., 2011, MNRAS, 414, 1965
- McHardy, I. M., Papadakis, I. E., Uttley, P. et al. 2004, MNRAS, 348, 783
- Muñoz-Darias, T., Casares, J., & Martínez-Pais, I. G. 2008, MNRAS, 385, 2205
- Nardini E., Reeves J. N., Porquet D., Braito V., Grosso N., Gofford J., 2014, MNRAS, 440, 1200
- Nikołajuk M., Czerny B., Gurynowicz P., 2009, MNRAS, 394, 2141
- Ninkov, Z., Walker, G. A. H., & Yang, S. 1987, ApJ, 321, 425
- Ochmann M. W., Kollatschny W., Zetzl M., 2020, Contrib. Astron. Obs. Skalnaté Pleso, 50, 318
- Oknyansky V., 2022, Astron. Nachr., 343, e210080
- Oknyansky V. L., Winkler H., Tsygankov S. S. et al. 2019, MNRAS, 483, 558
- Oknyansky V. L. et al., 2020, MNRAS, 498, 718
- Orosz, J. A. 2003, in IAU Symp. 212, A Massive Star Odyssey: From Main Sequence to Supernova, ed. K. van der Hucht, A. Herrero, & E. César (San Francisco, CA: ASP), 365
- Parmar, A. N., et al. 1997, A&AS, 122, 309

- Park, S. Q., et al. 2004, ApJ, 610, 378
- Parker M. L. et al., 2019, MNRAS, 483, L88
- Parker, M. L., Schartel, N., Grupe, D. et al. 2019, MNRAS, 483, L88
- Pastoriza, M., & Gerola, H. 1970, *Astrophys. Lett.*, 6, 155
- Penston, M. V., & Perez, E. 1984, MNRAS, 211, 33
- Peterson B. M., et al., 2004, ApJ, 613, 682
- Petrucci, P.-O. , Paltani, S., Malzac, J. et al., 2013, A&A 549, A73
- Poole, T. S., Breeveld, A. A., Page M. J. et al. 2008, MNRAS, 383, 627
- Pounds, K. A. & King, A. R., 2013, MNRAS, 433, 1369
- Remillard, R. A., & McClintock, J. E. 2006, ARA&A, 44, 49
- Ricci C., Ueda Y., Koss M. J. et al. 2015, ApJ, 815, L13
- Ricci, C., Ueda, Y., Paltani, S., et al., 2014, MNRAS, 441, 3622
- Ricci C., Paltani S., Ueda Y., Awaki H., 2013, MNRAS, 435, 1840
- Risaliti, G., 2002a A&A, 386, 379
- Risaliti, G., Elvis, M., Nicastro, F., 2002b, ApJ, 571, 234
- Rodriguez-Ardila, A., Fonseca-Faria, M. A., Denimara, D. dos S. et al., 2024, AJ, 167, 244
- Runnoe, J. C., Cales, S., Ruan, J. J. et al. 2016, MNRAS, 455, 1691
- Ruan, J. J., Anderson, S. F., Eracleous, M. et al. 2019, arXiv-prints, arXiv:1909.04676
- Sani E., Lutz D., Risaliti G. et el. 2010, MNRAS, 403, 1246
- Seifina, E., 2023, *Astron. Astrophys. Transact.*, Arxiv:2311.14830[astro-ph.GA]
- Seifina, E., Titarchuk, L., and Ugolkova, L., 2018am A&A, 619, 21
- Seifina E., Chekhtman A., Titarchuk L., 2018, A&A, 613, 48
- Seifina, E., Titarchuk, L., and Virgilli, E., 2017, A&A, 607, 38
- Seifina, E. V., 1999, *Astron. Rep.*, 43, 305

- Shakura, N. I., and Sunyaev, R. A., 1973, *A&A*, 24, 337
- Shaposhnikov, N., and Titarchuk, L., 2009, *A&A*, 699, 453
- Shara, M. M. & Hurley, J. R. 2002 *ApJ*, 571, 830
- Shobbrook R. R., 1966, *MNRAS*, 131, 365
- Shrader, Ch. & Titarchuk, L. 1999, *ApJ* 521, L121
- Smith, D.A. & Done, C., 1996, *MNRAS*, 280, 355
- Sniegowska, M., Grzedzielski, M., Czerny, B., & Janiuk, A. 2022, *Astron. Nachr.*, 343, e210065
- Springob, Ch. M., Haynes, M. P., Giovanelli, R., Kent, B. R., 2005, *ApJS*, 160, 149
- Sunyaev, R. A., & Titarchuk, L. G. 1980, *A&A*, 86, 121
- Tanaka Y., Inoue H., Holt S. S., 1994, *PASJ* 46, L37
- Terashima, Y., Gallo, L. C., Inoue, H., 2009, *Publ. Astron. Soc. Japan*, 61, S299
- Titarchuk, L. & Seifina, E., 2024, *Front. Astron. Space Sci.* 11:1368633
- Titarchuk, L., Seifina, E., and Shrader, Ch., 2023, *A&A*, 671, A159
- Titarchuk, L., and Seifina, E. 2023, *A&A*, 669, 57
- Titarchuk, L., and Seifina, E., 2021, *MNRAS*, 501, 5659
- Titarchuk L., Seifina E., Chekhtman A., and Ocampo, I., 2020, *A&A*, 633, A73
- Titarchuk, L., and Seifina, E. (2017). BL Lacertae: X-ray spectral evolution and a black-hole mass estimate. *Astron. Astrophys.* 602, 113
- Titarchuk, L., and Seifina, E., 2016a *A&A*, 585, A94
- Titarchuk, L., and Seifina, E., 2016b, *A&A*, 595, 110
- Titarchuk, L., Seifina, E., and Shaposhnikov, N., 2014, *ApJ*, 789, 57
- Titarchuk, L., Shaposhnikov, N., and Seifina, E., 2010, *AIP Conf. Proc.* 1205, 168
- Titarchuk, L., and Seifina, E., 2009, *ApJ*, 706, 1463
- Titarchuk, L. & Zannias, T. 1998, *ApJ*, 499, 315



- Titarchuk, Mastichiadis & Kylafis 1997, ApJ, 487, 834
- Titarchuk 1994, ApJ 434, 313
- Tripathi, P. & Dewangan, G. Ch., 2022, ApJ, 930, 117
- Tripathi, P. & Dewangan, G. Ch., 2022, ApJ, 925, 101
- Turner, T.J., George, I.M., Nandra, K., Mushotzky, R.F., 1997, ApJ, 488, 164
- Véron-Cetty, M. -P. & Véron, P., 2006, A&A, 455, 773
- Weng, Sh.-Sh., Chen, Y., Wang, T.-T. et al., 2020, MNRAS, 491, 2576
- Woo J.-H., Urry C. M., 2002, ApJ, 579, 530
- Wright, E. L. 2006, Publ. Astron. Soc. Pac., 118, 1711
- Xu, Y., Pinto, C., Bianchi, S. et al., 2021, NNRAS, 508, 6049
- Yankulova, I. M.; Golev, V. K.; Jockers, K. 2007, A&A, 469, 891
- Zhou X.-L., Wang J.-M., 2005, ApJL, 618, L83
- Zdziarski, A. A., Johnson, W. N., Magdziarz, P., 1996, MNRAS, 283, 193
- Zoghbi, A., Uttley, P. & Fabian, A. C. 2011, MNRAS, 412, 59
- Zoghbi A., Fabian A. C., Uttley P. et al. 2010, MNRAS, 401, 2419

## A. Tables

Table 1: Basic information on 1H 0707–495, NGC 1566 and NGC 7679

Source parameter	1H 0707–495	NGC 1566	Mrk 3	NGC 7679
Class of AGN	Sy1, NLS1 <sup>(a)</sup>	CL-AGN, SAB(s)bc <sup>(b)</sup>	Sy2, S0, HBLR <sup>(c)</sup>	Sy2, SB0, SB+AGN
Mass of BH, $M_{\odot}$	$2 \times 10^6$ – $10^7$ <sup>(d)</sup>	$8.3 \times 10^6$ – $1.3 \times 10^7$ <sup>(e,f)</sup>	$5.5 \times 10^8$ <sup>(g)</sup>	$5.9 \times 10^6$ <sup>(h)</sup>
Inclination, $i$ , deg	55–65 <sup>(i)</sup>	$60 \pm 5$ <sup>(j)</sup> ,	50 <sup>(c)</sup>	30 <sup>(k)</sup>
Distance, $D$ , Mpc	160 <sup>(l)</sup>	21.3 <sup>(m)</sup>	63.2 <sup>(c)</sup>	$58.633 \pm 1.910$ <sup>(k)</sup>
Redshift, $z$	0.041 <sup>(d)</sup>	0.005 <sup>(j,m)</sup>	0.013 <sup>(c)</sup>	0.017 <sup>(d)</sup>
RA (J2000), $\alpha$	07 <sup>h</sup> 08 <sup>m</sup> 41.48 <sup>s</sup> <sup>(l)</sup>	04 <sup>h</sup> 20 <sup>m</sup> 00.52 <sup>s</sup> <sup>(l)</sup>	06 <sup>h</sup> 15 <sup>m</sup> 36.3 <sup>s</sup> <sup>(l)</sup>	23 <sup>h</sup> 28 <sup>m</sup> 46.73 <sup>s</sup> <sup>(l)</sup>
Dec (J2000), $\delta$	–49° 33′ 06.4″ <sup>(l)</sup>	–54° 56′ 17.1″ <sup>(l)</sup>	+71° 2′ 15″ <sup>(l)</sup>	+03° 30′ 42.1″ <sup>(l)</sup>
Mean count rate, ct/s	$0.1975 \pm 0.0013$ <sup>(l)</sup>	$0.2984 \pm 0.0013$ <sup>(l)</sup>	$0.192 \pm 0.012$ <sup>(l)</sup>	$0.192 \pm 0.012$ <sup>(l)</sup>
Mean flux, $\times 10^{-12}$ erg/s/cm <sup>2</sup>	$4.533 \pm 0.030$ <sup>(l)</sup>	$11.74 \pm 0.05$ <sup>(l)</sup>	$9.7 \pm 0.7$ <sup>(l)</sup>	$7.9 \pm 0.5$ <sup>(l)</sup>
Swift name, 2SXPS...	J070841.4–493306	J0420.0–5457	J061536.2+710214	J232846.7+033042
Alternative names	1H 0659–494, 4U 0708–49	ESO 157–20, IRAS 04189–5503, PGC 14897	UGC 03426	Arp 216, Mrk 534, PGC 71554, VV 329a, UGC 12618
$N_{H,Gal}$ , cm <sup>–2</sup>	$8.0 \times 10^{20}$ <sup>(k)</sup>	$1.1 \times 10^{20}$ <sup>(k)</sup>	$1.8 \times 10^{20}$ <sup>(l)</sup>	$4.5 \times 10^{20}$ <sup>(m)</sup>

NLS1 – Narrow-line Seyfert 1 galaxy; SAB(s)bc – barred spiral galaxy; CL-AGN – changing-look AGN; SB0 – early-type barred galaxy; S0 – lenticular galaxy; HBLR – hidden broad-line-region; Mean count rate and flux of the source is measured in 0.3–10 keV range. <sup>(a)</sup> Zoghbi et al. (2011); <sup>(b)</sup> de Vaucouleurs (1973); Shobbrook (1966), de Vaucouleurs (1991); <sup>(c)</sup> Véron-Cetty & Véron (2006); Ricci et al. (2014); <sup>(d)</sup> Zhou & Wang (2005); Kara et al. (2013); Done & Jin (2016); Zoghbi et al. (2011); <sup>(e)</sup> Woo & Urry (2002); <sup>(f)</sup> Elagali et al. (2019); <sup>(g)</sup> Fabian et al. (2009); <sup>(h)</sup> Hancock et al. (2023); <sup>(i)</sup> Aguero et al. (2004); <sup>(j)</sup> Kewley et al. (2001); Springob et al. (2005); <sup>(k)</sup> Galactic neutral hydrogen column density along the line of sight from the Leiden/Dwingeloo Survey Hartman & Burton (1997); <sup>(l)</sup> <https://www.swift.ac.uk/2SXPS/>; and <sup>(m)</sup> Della Ceca et al. (2001).

Table 2: Details of *Suzaku*, *ASCA*, *BeppoSAX*, *RXTE*, *NuSTAR* and *XMM-Newton* observations of AGNs.

Source	Epoch	Mission	Obs. ID	Start time (UT)	End time (UT)	MJD interval
1H 0707	A1	ASCA	73043000	1995 Mar 15 23:01:26	1995 Mar 17 03:00:19	49792.0–49793.1 <sup>1</sup>
	A2	ASCA	76031000	1998 May 16 19:24:15	1998 May 20 07:10:38	50949.8–50953.3
	A3	ASCA	87043000	1999 Mar 13 00:23:59	1999 Mar 14 14:48:30	51250.0–51251.6
	Sz1	<i>Suzaku</i>	700008010	2005 Dec 3 04:13:19	2005 Dec 6 02:20:20	50873.0–50873.5 <sup>1</sup>
	R1	RXTE	20309010100	1997 Mar 15 06:03:28	1997 Mar 15 13:01:36	50522.2–50522.6
NGC 1566	Sz2	<i>Suzaku</i>	707002010	2012 May 19 01:36:44	2012 May 20 06:34:19	56066.3–56067.2 <sup>2</sup>
	Ns1	<i>NuSTAR</i>	80301601002	2018 June 26 20:06:09	2018 June 28 02:21:07	58295.8–58297.0 <sup>2</sup>
	Xn1	<i>XMM-Newton</i>	0800840201	2018 June 27 00:13:32	2018 June 28 02:00:33	58296.0–58297.0 <sup>2</sup>
	Ns2	<i>NuSTAR</i>	80401601002	2018 Oct 4 12:16:09	2018 Oct 6 06:24:57	58395.5–58397.2 <sup>2</sup>
	Xn2	<i>XMM-Newton</i>	0820530401	2018 Oct 4 12:52:23	2018 Oct 5 18:29:26	58395.5–58396.7 <sup>2</sup>
	Ns3	<i>NuSTAR</i>	80502606002	2019 June 5 07:46:09	2019 June 6 16:09:57	58639.3–58640.6 <sup>2</sup>
	Xn3	<i>XMM-Newton</i>	0840800401	2019 June 5 08:11:23	2019 June 6 09:55:03	58639.3–58640.4 <sup>2</sup>
	Ns4	<i>NuSTAR</i>	60501031002	2019 Aug 8 11:26:09	2019 Aug 9 16:29:57	58703.4–58704.6 <sup>2</sup>
	Xn4	<i>XMM-Newton</i>	0851980101	2019 Aug 11 16:45:53	2019 Aug 11 16:53:37	58706.6–58706.7 <sup>2</sup>
	Ns5	<i>NuSTAR</i>	60501031004	2019 Aug 18 05:01:09	2019 Aug 19 18:19:57	58713.2–58714.7 <sup>2</sup>
Ns6	<i>NuSTAR</i>	60501031006	2019 Aug 21 10:21:09	2019 Aug 23 03:41:11	58716.4–58718.1 <sup>2</sup>	
NGC 7679	A4	ASCA	66019000	1998 July 1 15:52:42	1998 July 3 10:30:42	50995.6–50997.4 <sup>3</sup>
	A5	ASCA	66019010	1999 June 13 23:33:07	1999 June 14 13:38:03	51342.9–51343.6 <sup>3</sup>
	B1	<i>BeppoSAX</i>	40631001	1998 Dec 6 15:27:33	1998 Dec 9 03:39:11	51153.6–51156.2 <sup>3</sup>
Mrk 3	A6	ASCA	70002000	1993 Apr 21 06:27:06	1993 Apr 22 03:00:58	49098.2–49099.1 <sup>4</sup>
	A7	ASCA	74041000	1996 Oct 26 14:02:48	1996 Oct 27 03:50:10	50382.5–50383.1 <sup>4</sup>
	R2	RXTE	20330010100	1996 Dec 25 16:17:04	1996 Dec 25 17:39:44	50442.6–50442.7 <sup>4</sup>
	R3	RXTE	20330011000	1997 Feb 17 05:17:29	1997 Feb 17 07:10:40	50496.2–50496.3 <sup>4</sup>
	R4	RXTE	20330010900	1997 Mar 16 13:03:44	1997 Mar 16 15:14:40	50523.5–50523.6 <sup>4</sup>
	R5	RXTE	20330010800	1997 Mar 21 08:06:40	1997 Mar 21 10:07:44	50528.3–50528.4 <sup>4</sup>
	R6	RXTE	20330010700	1997 Mar 31 05:30:08	1997 Mar 31 07:20:48	50538.2–50538.3 <sup>4</sup>
	R7	RXTE	20330010600	1997 Apr 4 00:22:40	1997 Apr 4 11:13:04	50542.0–50542.4 <sup>4</sup>
	R8	RXTE	20330010300	1997 Apr 15 06:53:36	1997 Apr 15 08:44:32	50553.2–50553.3 <sup>4</sup>
	R9	RXTE	20330010200	1997 Apr 14 08:28:32	1997 Apr 14 10:07:44	50552.3–50552.4 <sup>4</sup>
	R10	RXTE	20330010400	1997 Apr 16 01:17:20	1997 Apr 16 02:24:32	50554.0–50554.1 <sup>4</sup>
	R11	RXTE	20330010500	1997 Apr 17 09:09:20	1997 Apr 17 11:13:04	50555.3–50555.4 <sup>4</sup>
	R12	RXTE	20330011100	1997 May 30 19:40:32	1997 May 30 21:31:44	50598.8–50598.9 <sup>4</sup>
	R13	RXTE	20330011200	1997 July 7 01:01:20	1997 July 7 02:57:36	50636.0–50636.1 <sup>4</sup>
	B2	<i>BeppoSAX</i>	50132002	1997 Apr 16 14:46:38	1997 Apr 18 10:21:50	50554.6–50556.4 <sup>4</sup>
Sz3	<i>Suzaku</i>	100040010	2005 Oct 22 02:02:09	2005 Oct 24 06:26:14	53665.1–53667.2 <sup>1</sup>	
Sz4	<i>Suzaku</i>	709022010	2014 Oct 1 22:08:01	2014 Oct 2 10:02:09	56931.9–56932.4 <sup>4</sup>	
Sz5	<i>Suzaku</i>	709022020	2014 Oct 7 19:20:38	2014 Oct 8 01:48:17	56937.8–56938.1 <sup>4</sup>	
Sz6	<i>Suzaku</i>	709022030	2014 Oct 23 03:37:31	2014 Oct 23 16:09:23	56953.2–56953.7 <sup>4</sup>	
Sz7	<i>Suzaku</i>	709022040	2015 Mar 23 05:48:56	2015 Mar 23 15:02:23	57104.2–57104.6	
Sz8	<i>Suzaku</i>	709022050	2015 Apr 4 11:21:15	2015 Apr 4 23:42:19	57116.4–57116.9	

Columns 1 – 7 denote Source name, Epoch, Observation ID, Mission Name, Start time (UT), End time (UT), MJD interval, respectively. See the text for details. (1) Zoghbi et al. (2011); (2) Jana et al. (2021); Oknyansky et al. (2019, 2020); Tripathi & Dewangan (2022a); (3) Della Ceca et al. (2001); (4) Griffiths et al. (1998); Georgantopoulos et al. (1999); Matt et al. (2000); Ricci et al. (2014).

Table 3: Details of *Swift* observations of 1H 0707–495, NGC 1566, NGC 7679 and Mrk 3.

Source	Observation ID	Start time (UT)	End time (UT)	MJD interval
1H 0707–495	00090393(001-023,025-063, 065-068,070-075,077-085, 087-091,093-105)	Apr 3, 2010	Apr 30, 2018	55289 – 58238
	0004031700(1,3)	Dec 22, 2010 18:43:44	Jan 27, 2011 12:08:54	55552.78 – 55588.50
	0009162300(1,2)	May 19, 2013	June 19, 2013	56431.34 – 56462.05
	000807200(01-13,15-16,19-59)	May 5, 2014	Jan 31, 2018	56782 – 58150
NGC 1566	00035880(002-004,006,046-051, 053-072,084-089, 092,094-117, 119,137-144)	Dec 12, 2007	July 31, 2019	54446 – 58695 <sup>1,2</sup>
	000317420(01,03-13,15)	June 23, 2010	Oct 21, 2020	55370 – 59143 <sup>1,2</sup>
	000456040(01,02,04-08,10-17, 20-28,31-33,35-51)	Aug 25, 2011	Nov 2, 2023	55798 – 60250
	000334110(01-05,07-09,11-30)	Sep 11, 2014	July 30, 2015	56911 – 57233 <sup>1,2</sup>
	0008891000(1-3)	Aug 8, 2019 <sup>1,3</sup>	Aug 19, 2021	58703 – 58716 <sup>1</sup>
	000149160(01,03-19,21-29)	Nov 11, 2021	Jan 17, 2022	59529 – 59596
	0311166600(1-9)	June 21, 2022	Aug 19, 2022	59751 – 59810
	0001492300(1,2)	Nov 19, 2021 00:02:52	Nov 19, 2021 00:04:54	59537.001 – 59537.003
	0001530200(1-4)	Aug 19, 2022	Aug 22, 2022	59814 – 59817
	NGC 7679	00088108002	Oct 6, 2017 10:00:34	Oct 6, 2017 10:280:35
03105479004		Jan 16, 2019 13:51:34	Jan 16, 2019 10:16:33	58499.577 – 58499.580
0003546000(1-5,7-8)		Mar 21, 2006	May 6, 2012	53815.3 – 56053.1
Mrk 3	00037226001	Jan 22, 2008 00:40:07	Jan 22, 2008 02:37:05	54487.0 – 54487.1
	0008036800(1- 6,8-10)	Sep 7, 2014	Apr 20, 2015	56907.7 – 57132.7

Columns 1 – 5 denote Source name, Observation ID, Start time (UT), End time (UT), MJD interval, respectively. See the text for details. (1) Jana et al. (2021) and (2) Oknyansky (2022).

Table 4: Best-fit parameters of spectral analysis of ASCA, *Suzaku* (shaded in gray), *BeppoSAX* (shaded in blue), *NuSTAR* (shaded in red), RXTE (shaded in green) and *XMM-Newton* (shaded in yellow) observations of AGNs <sup>†</sup>.

Obs. ID	MJD, day	$\alpha =$ $\Gamma - 1$	$T_s,$ keV	$\log(A)$	$N_{com}^{\ddagger}$	$E_{line},$ keV	$N_{line}^{\ddagger\ddagger}$	$\chi_{red}^2$ (dof)
1H 0707–495								
73043000	49792.0	1.03±0.09	0.107±0.004	-1.14±0.07	2.31±0.9	0.83±0.09	11.02±0.04	1.01(86)
76031000	50949.8	0.43±0.10	0.111±0.005	-1.30±0.09	0.75±0.3	0.84±0.05	2.12±0.06	1.19(80)
87043000	51250.0	1.20±0.10	0.065±0.004	-1.06±0.03	8.39±0.6	0.82±0.08	5.37±0.02	1.04(69)
700008010	53707.355	0.79±0.13	0.121±0.004	-1.14±0.05	7.6±0.2	0.83±0.02	1.04±0.02	1.00(802)
NGC 1566								
707002010	56066.3	0.77±0.04	0.13±0.01	0.42±0.04	0.22±0.03	6.36±0.04	0.096±0.003	0.95(563)
80301601002	58295.8	1.01±0.03	0.14±0.02	0.12±0.02	1.07±0.04	6.36±0.05	0.098±0.007	0.99(963)
0800840201	58296.0	1.05±0.04	0.13±0.01	0.11±0.05	1.11±0.05	6.37±0.06	0.095±0.009	0.99(430)
80401601002	58395.5	0.95±0.06	0.14±0.03	0.18±0.09	0.26±0.07	6.5±0.1	0.08±0.01	1.04(968)
0820530401	58395.5	0.92±0.04	0.13±0.01	0.18±0.05	0.26±0.05	6.37±0.06	0.095±0.009	0.99(430)
80502606002	58639.3	1.15±0.06	0.14±0.03	0.42±0.09	0.34±0.07	6.5±0.1	0.08±0.01	1.04(968)
0840800401	58639.3	1.12±0.05	0.15±0.02	0.20±0.04	0.57±0.06	6.4±0.07	0.09±0.02	1.02(435)
60501031002	58703.4	0.89±0.05	0.14±0.03	0.61±0.05	0.37±0.05	6.46±0.03	0.096±0.003	0.89(831)
0851980101	58706.6	0.85±0.06	0.13±0.02	0.64±0.04	0.29±0.04	6.42±0.09	0.096±0.003	0.97(210)
60501031004	58713.2	0.75±0.09	0.13±0.01	0.62±0.03	0.35±0.03	6.43±0.05	0.096±0.003	0.93(723)
60501031006	58716.4	0.65±0.07	0.14±0.03	0.72±0.05	0.21±0.06	6.40±0.06	0.096±0.003	0.87(722)
NGC 7679								
66019000	50995.6	0.62±0.02	0.15±0.07	2.00 <sup>†††</sup>	0.30±0.01	6.5±0.1	0.21±0.01	1.09(145)
66019010	51432.9	0.55±0.04	0.13±0.04	0.08±0.01	0.37±0.02	6.41±0.09	0.41±0.02	0.97(66)
40631001	51153.6	0.60±0.02	0.35±0.06	0.26±0.03	0.71±0.03	6.4±0.5	0.075±0.02	1.04(82)
Mrk 3								
70002000	49098.2	0.10±0.02	0.18±0.01	-1.43±0.02	0.001±0.001	6.41±0.09	0.54±0.06	1.05(52)
74041000	50382.5	0.10±0.02	0.21±0.01	-1.59±0.03	0.002±0.001	6.39±0.07	0.63±0.02	1.09(41)
20330010100	50442.6	0.21±0.02	0.28±0.01	-3.47±0.04	0.46±0.89	6.41±0.08	1.99±0.09	0.83(47)
20330010200	50552.3	0.54±0.02	0.29±0.02	-3.40±0.05	1.21±0.18	6.42±0.05	1.9±0.2	0.92(47)
20330010300	50553.2	0.31±0.02	0.28±0.02	-3.25±0.06	0.63±0.09	6.41±0.06	2.4±0.6	0.93(47)
20330010400	50554.0	0.82±0.03	0.31±0.05	-2.91±0.09	0.54±0.06	6.41±0.07	2.8±0.3	1.04(47)
20330010500	50555.3	0.17±0.02	0.28±0.02	-3.06±0.08	0.44±0.07	6.35±0.09	1.73±0.09	0.89(47)
20330010600	50542.0	1.02±0.03	0.23±0.02	-2.82±0.08	0.59±0.07	6.37±0.08	3.83±0.08	1.10(47)
20330010700	50538.2	0.87±0.02	0.31±0.03	-3.15±0.07	1.05±0.19	6.42±0.04	3.93±0.09	0.96(47)
20330010800	50528.3	0.21±0.02	0.29±0.03	-3.28±0.09	0.67±0.17	6.39±0.05	2.99±0.08	0.94(47)
20330010900	50523.5	0.11±0.01	0.30±0.02	-2.79±0.11	0.55±0.07	6.38±0.08	2.20±0.09	0.86(47)
20330011000	50496.2	0.95±0.02	0.28±0.01	-2.56±0.11	0.20±0.07	6.39±0.09	4.33±0.08	0.94(47)
20330011100	50598.8	0.50±0.02	0.24±0.01	-2.33±0.11	0.03±0.07	6.40±0.06	1.84±0.05	0.89(47)
20330011200	50636.0	0.51±0.01	0.31±0.03	-3.19±0.16	0.30±0.04	6.40±0.07	2.55±0.09	0.98(47)
50132002	50554.6	0.55±0.04	0.23±0.03	-2.83±0.16	0.04±0.01	6.40±0.08	0.68±0.04	0.90(84)
100040010	53665.1	0.10±0.02	0.10±0.01	-0.47±0.02	0.0001±0.0001	6.41±0.05	0.54±0.06	0.94(629)
709022010	56931.9	0.11±0.01	0.10±0.01	-0.90±0.02	0.0011±0.0001	6.41±0.02	1.03±0.01	0.98(238)
709022020	56937.8	0.09±0.02	0.13±0.01	0.27±0.02	0.00015±0.0001	6.50±0.08	5.06±0.01	1.05(258)
709022030	56953.2	0.10±0.02	0.14±0.01	0.53±0.02	0.00014±0.0001	6.57±0.09	5.31±0.01	1.02(300)
709022040	57104.2	0.11±0.03	0.16±0.01	0.02±0.01	0.00003±0.0001	6.48±0.07	3.62±0.01	1.54(293)
709022050	57116.4	0.10±0.01	0.15±0.02	-0.03±0.01	0.00003±0.0001	6.49±0.04	3.15±0.01	1.47(154)

Parameter errors correspond to  $1\sigma$  confidence level. <sup>†</sup> The spectral model is *tbabs\*(BMC + Gaussian/Laor)*. <sup>††</sup> Normalization parameters of *BMC* component is in units of  $L_{35}^{soft}/d_{10}^2$ , *erg/s/kpc*<sup>2</sup>, where  $L_{35}^{soft}$  is the soft photon luminosity in units of  $10^{35}$ ;  $d_{10}$  is the distance to the source in units of 10 kpc. <sup>†††</sup> *Gaussian/Laor* component is in units of  $10^{-4} \times$  total photons  $\text{cm}^{-2}\text{s}^{-1}$ . <sup>††††</sup> When parameter  $\log(A) > 1$ , it is fixed to a value 2.0 (see comments in the text).  $N_H$  was fixed at the value  $2.5 \times 10^{20} \text{ cm}^{-3}$  (for NGC 1566),  $3 \times 10^{21} \text{ cm}^{-3}$  (for 1H 0707) and  $4 \times 10^{21} \text{ cm}^{-3}$  (for NGC 7679).

For 1H 0707 we presented the strongest *Laor*-line component among all line features in the source spectrum, although we used the full composition of N XVII, O III, Fe XVII, Ne X, S XVI, Fe I–XXII and Fe XXV/Fe XXVI  $K_\alpha$  lines with energies of 0.5, 0.65, 0.85, 1.02, 2.9, 6.4 and 6.8 keV, respectively.

Table 5: BH mass scaling for 1H 0707–495.

Reference sources	$m_r, M_\odot$	$i_r^{(a)}, \text{deg}$	$N_r, L_{39}/d_{10}^2$	$d_r^{(b)}, \text{kpc}$
HLX–1 ESO 243–49 <sup>(1)</sup>	$(7.2 \pm 0.7) \times 10^4$	75	$4.2 \times 10^{-6}$	$95 \pm 10$
M101 ULX–1 <sup>(2)</sup>	$(3.7 \pm 0.6) \times 10^4$	18	$3 \times 10^{-4}$	$6.9 \pm 0.7$
OJ 287 <sup>(3)</sup>	$(1.25 \pm 0.5) \times 10^8$	50	$2.4 \times 10^{-4}$	$1037 \pm 10$
SDSS J0752 <sup>(4)</sup>	$\sim 9 \times (1 \pm 0.31) \times 10^7$	70	$1.1 \times 10^{-2}$	$\sim 500$

Target source	$m_t (M_\odot)$	$i_t^{(a)} (\text{deg})$	$d_t^{(b)} (\text{Mpc})$
	$M_\odot$	deg	Mpc
1H 0707	$\sim 6.8 \times (1 \pm 0.45) \times 10^7$	55	160 that using ESO 243-49 as a ref. source
1H 0707	$\sim 6.8 \times (1 \pm 0.45) \times 10^7$	55	160 that using M101 ULX-1 as a ref. source
1H 0707	$\sim 6.8 \times (1 \pm 0.45) \times 10^7$	55	160 that using OJ 287 as a ref. source
1H 0707	$\sim 6.8 \times (1 \pm 0.45) \times 10^7$	55	160 that using SDSS J0752 as a ref. source
1H 0707	Final estimate	55	160 as a standard deviation for a mean:
	$\sim 6.8 \times (1 \pm 0.27) \times 10^7$		$0.45/4^{1/2} = 0.27$

(a) System inclination in the literature and (b) source distance found in the literature. (1) Titarchuk and Seifina (2016b); (2) Titarchuk and Seifina (2016a); and (3) Titarchuk et al. (2023).

Table 6: BH mass scaling for NGC 1566 and NGC 7679.

Reference sources	$m_r, M_\odot$	$i_r^{(a)}, \text{deg}$	$N_r, L_{39}/d_{10}^2$	$d_r^{(b)}, \text{kpc}$
NGC 4051 <sup>(1)</sup>	$6 \times 10^5$	50	$9 \times 10^{-4}$	9800
GX 339–4 <sup>(2)</sup>	$\sim 6$	...	$5.1 \times 10^{-2}$	$7.5 \pm 1.6$
GRO J1655–40 <sup>(3)</sup>	$6.3 \pm 0.3$	$70 \pm 1$	$5.2 \times 10^{-2}$	$3.2 \pm 0.2$
Cyg X–1 <sup>(4)</sup>	6.8–13.3	$35 \pm 5$	0.9	$2.5 \pm 0.3$
4U 1543–47 <sup>(5)</sup>	$\sim 11$	$20.7 \pm 1.5$	0.12	$7.5 \pm 1$
Target source	$m_r, M_\odot$	$i_r^{(a)}, \text{deg}$	$d_r^{(b)}, \text{Mpc}$	
NGC 1566	$\sim 1.9 \times (1 \pm 0.45) \times 10^5$	37.5	21.3	that using NGC 4051 as a ref. source
NGC 1566	$\sim 1.9 \times (1 \pm 0.45) \times 10^5$	37.5	21.3	that using GX 339–4 as a ref. source
NGC 1566	$\sim 1.9 \times (1 \pm 0.45) \times 10^5$	37.5	21.3	that using GRO J1655–40 as a ref. source
NGC 1566	$\sim 1.9 \times (1 \pm 0.45) \times 10^5$	37.5	21.3	that using Cyg X–1 as a ref. source
NGC 1566	$\sim 1.9 \times (1 \pm 0.45) \times 10^5$	37.5	21.3	that using 4U 1543–47 as a reference source
NGC 1566	Final estimate	37.52	21.3	as a standard deviation for a mean: $\sim 1.9 \times (1 \pm 0.20) \times 10^5$ $0.45/5^{1/2} = 0.20$
NGC 7679	$\sim 8.4 \times (1 \pm 0.45) \times 10^6$	30	57.28	that using NGC 4051 as a ref. source
NGC 7679	$\sim 8.4 \times (1 \pm 0.45) \times 10^6$	30	57.28	that using GX 339–4 as a ref. source
NGC 7679	$\sim 8.4 \times (1 \pm 0.45) \times 10^6$	30	57.28	that using GRO J1655–40 as a ref. source
NGC 7679	$\sim 8.4 \times (1 \pm 0.45) \times 10^6$	30	57.28	that using Cyg X–1 as a ref. source
NGC 7679	$\sim 8.4 \times (1 \pm 0.45) \times 10^6$	30	57.28	that using 4U 1543–47 as a reference source
NGC 7679	Final estimate	30	57.28	as a standard deviation for a mean: $\sim 8.4 \times (1 \pm 0.20) \times 10^6$ $0.45/5^{1/2} = 0.20$
Mrk 3	$\sim 2.2 \times (1 \pm 0.45) \times 10^8$	50	63.2	that using NGC 4051 as a ref. source
Mrk 3	$\sim 2.2 \times (1 \pm 0.45) \times 10^8$	50	63.2	that using GX 339–4 as a ref. source
Mrk 3	$\sim 2.2 \times (1 \pm 0.45) \times 10^8$	50	63.2	that using GRO J1655–40 as a ref. source
Mrk 3	$\sim 2.2 \times (1 \pm 0.45) \times 10^8$	50	63.2	that using Cyg X–1 as a ref. source
Mrk 3	$\sim 2.2 \times (1 \pm 0.45) \times 10^8$	50	63.2	that using 4U 1543–47 as a reference source
Mrk 3	Final estimate	50	63.2	as a standard deviation for a mean: $\sim 2.2 \times (1 \pm 0.20) \times 10^8$ $0.45/5^{1/2} = 0.20$

(a) System inclination in the literature and (b) source distance found in the literature. (1)

Christopoulou et al. (1997); McHardy et al. (2004); Haba et al. (2008); Pounds & King (2013); Lobban et al. (2011); Terashimai et al. (2009); Denney et al. (2009); Seifina et al. (2018b); (2) Munoz-Darias et al. (2008); Hynes et al. (2004) (3) Greene et al. (2001); Hjellming & Rupen (1995); (4) Herrero et al. (1995); Ninkov et al. (1987); and (5) Orosz (2003); Park et al. (2004).

Table 7: General properties of the Sy1 (left part), Sy2 (right part) and CL-AGN (indicated by yellow color) sample galaxies.

Sy1, CL-AGN source	$D^\dagger$ , Mpc	$M_{BH}$ , $\times 10^6 M_\odot$	$L_{x,44}^{\dagger\dagger}$	$\bar{\Gamma}$	Sy2 AGN source	$D^\dagger$ , Mpc	$M_{BH}$ , $\times 10^6 M_\odot$	$L_{x,40}^{\dagger\dagger}$	$\bar{\Gamma}$
NGC 7314 <sup>(1)</sup>	15.4	0.87	0.11	1.80±0.15	NGC 7679	58.6	8.4	3200	1.60±0.06
NGC 3227 <sup>(2,3)</sup>	20.4	42.2	0.19	1.65±0.12	Mrk 348 <sup>(13)</sup>	63.90	38.01	575.4	1.50±1.56
NGC 3516 <sup>(2,3)</sup>	37.5	42.7	0.62	1.63±0.12	NGC 424 <sup>(13)</sup>	47.60	60.5	54.95	1.49±0.90
NGC 4593 <sup>(2,3)</sup>	42.0	5.36	0.8	1.79±0.14	Mrk 573 <sup>(13)</sup>	71.30	23.44	44.6	2.50±2.78
NGC 3783 <sup>(2,3)</sup>	44.7	29.8	1.7	1.68±0.08	NGC 788 <sup>(13)</sup>	56.10	26.91	128.8	1.41±1.67
NGC 7469 <sup>(2,3,4)</sup>	62.7	12.2	1.47	1.84±0.10	ESO 417–G06 <sup>(13)</sup>	65.60	27.54	288.4	1.03±1.25
IC 4329A <sup>(2,3)</sup>	70.5	9.9	1.06	1.76±0.03	Mrk 1066 <sup>(13)</sup>	51.70	16.98	25.11	2.17±2.40
NGC 5548 <sup>(5)</sup>	74.5	52.2	2.9	1.69±0.12	3C 98.0 <sup>(13)</sup>	124.90	56.23	1348.9	1.04±0.81
Mrk 79 <sup>(2,6)</sup>	94.3	52.4	2.2	1.71±0.21	Mrk 3 <sup>(13)</sup>	63.20	549.54	173.7	1.25±1.33
Ark 120 <sup>(2,6)</sup>	138	150	7.6	1.73±0.17	Mrk 1210 <sup>(13)</sup>	53.60	50.12	204.4	1.01±1.40
Mrk 509 <sup>(2,3)</sup>	141	143	2.41	1.72±0.08	IC 2560 <sup>(13)</sup>	34.80	2.88	3.7	1.32±1.50
Fairall 9 <sup>(2,3)</sup>	198	255	10.1	1.84±0.18	NGC 3393 <sup>(13)</sup>	48.70	125.89	43.6	2.67±3.04
MR 2251-178 <sup>(7)</sup>	271	240	46.6	1.75±0.11	NGC 4507 <sup>(13)</sup>	46.00	181.97	109.6	1.62±1.70
NGC 4051 <sup>(2,3,8)</sup>	12.7	1.91	0.05	1.90±0.10	NGC 4698 <sup>(13)</sup>	23.40	33.88	1.38	2.16±1.98
NGC 5506 <sup>(3,9)</sup>	29.1	5.1	1.29	1.85±0.06	NGC 5194 <sup>(13)</sup>	7.85	5.37	0.34	2.68±3.01
MCG 63015 <sup>(10)</sup>	35.8	3.26	0.78	1.76±0.09	Mrk 268 <sup>(13)</sup>	161.50	89.12	21.8	2.11±3.07
Mrk 766 <sup>(11)</sup>	57.6	1.76	1.15	2.02±0.20	Circinus <sup>(13)</sup>	4.21	51.28	0.63	0.98±0.75
Ark 564 <sup>(12)</sup>	98.5	2.6	2.8	2.51±0.09	NGC 5643 <sup>(13)</sup>	16.90	1.99	2.75	0.99±1.42
Mrk 335 <sup>(2,6)</sup>	103	14.2	1.24	1.97±0.51	Mrk 477 <sup>(13)</sup>	156.70	15.84	398.1	1.10±1.48
Mrk 110 <sup>(2,6)</sup>	151	25.1	8.71	1.81±0.16	IC 4518A <sup>(13)</sup>	65.20	30.19	114.8	1.94±1.66
1H 0707-495	160	6.8	1.38	2.00±1.06	ESO 138–G01 <sup>(13)</sup>	36.00	0.31	169.8	2.31±2.40
NGC 1566	21.3	0.19	0.06	1.60±0.06	NGC 6300 <sup>(13)</sup>	14.43	15.13	20.89	1.00±0.99
Mrk 273 <sup>(1)</sup>	156.70	54.95	0.002	1.91±0.07	NGC 7172 <sup>(13)</sup>	33.90	158.48	316.2	1.52±1.58
NGC 7319 <sup>(1)</sup>	77.25	726.91	0.098	1.29±1.20	NGC 7212 <sup>(13)</sup>	111.80	34.67	64.56	1.07±0.47

<sup>†</sup> Luminosity distance ( $D$ ) are taken from the NED data base. <sup>††</sup>  $L_{x,44}$  and  $L_{x,40}$  are the soft photon luminosities in 2–10 keV energy range in units of  $10^{44}$  and  $10^{40}$  erg/s, respectively. <sup>(1)</sup> Gu et al.

(2006), Elvis et al. (1994); <sup>(2)</sup> Peterson et al. (2004); <sup>(3)</sup> Ricci et al. (2013); <sup>(4)</sup> Seifina et al. (2018a); <sup>(5)</sup> Bentz & Katz (2015); <sup>(6)</sup> Woo & Urry (2002); <sup>(7)</sup> Dunn et al. (2014); <sup>(8)</sup> Titarchuk et al. (2020); <sup>(9)</sup> Nikolajuk et al. (2009); <sup>(10)</sup> Hu et al. (2016); <sup>(11)</sup> Bentz et al. (2009); <sup>(12)</sup> Botte et al. (2004); and <sup>(13)</sup> Hernandez-Garca et al. (2015).



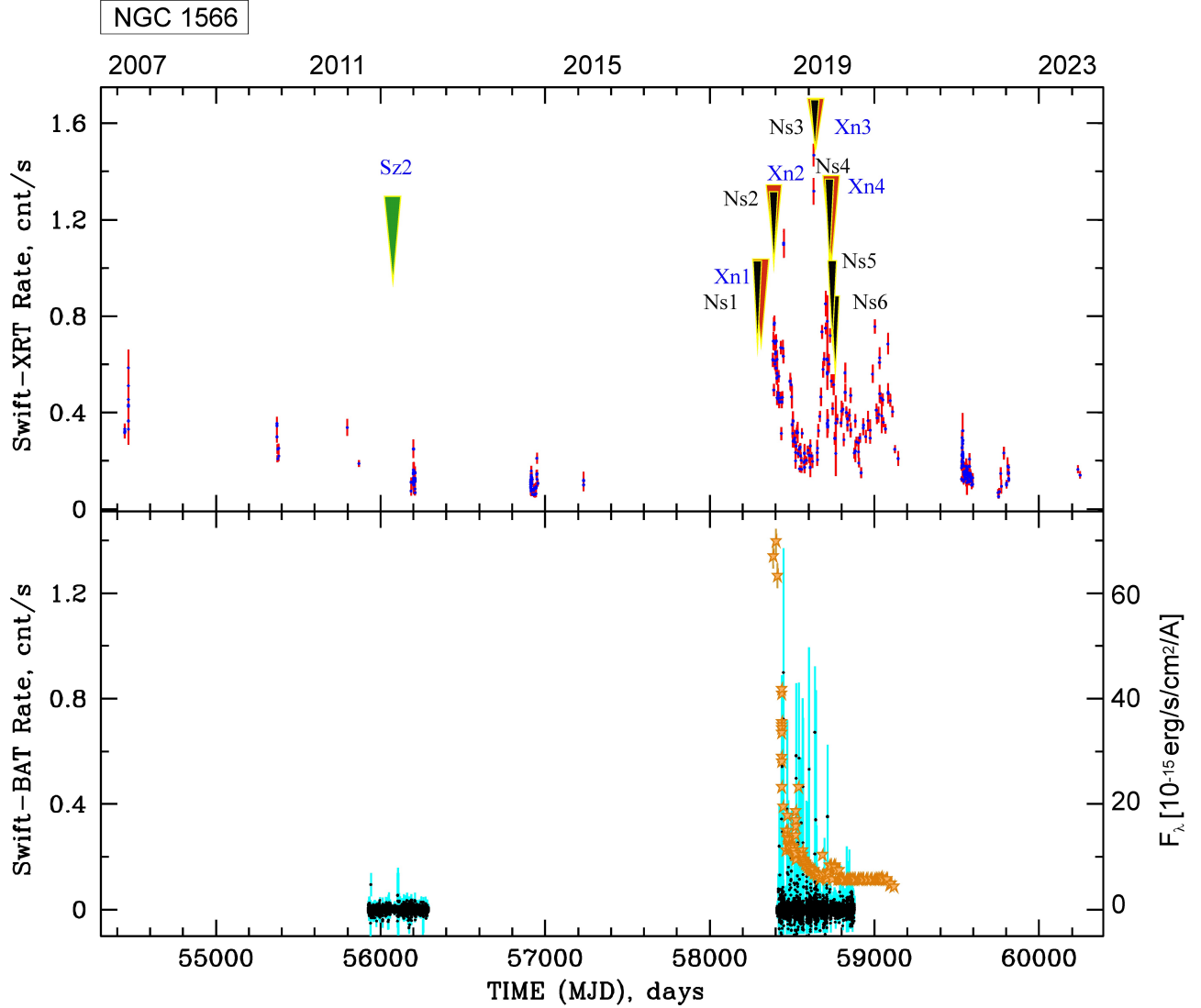


Fig. 1.— Evolution of NGC 1566 during 2007–2023 observations with Swift/XRT (top panel, 0.3–10 keV), Swift/BAT (bottom panel, black points, 15–150 keV) and Swift/UVOT (bottom panel, orange stars, UVW2 band [1600–2300 Å], right axis). Green, black and red triangles indicates *Suzaku*, *NuSTAR* and *XMM-Newton* observations, respectively, used for in our analysis.

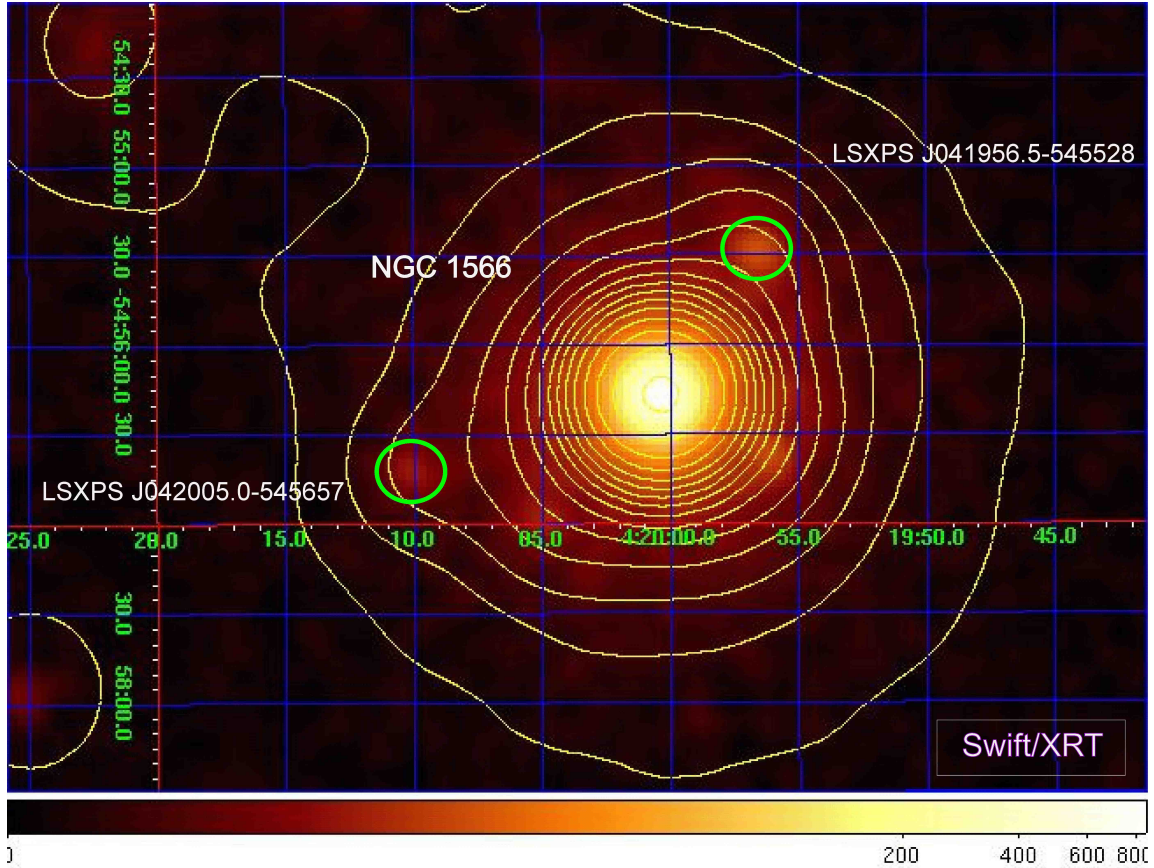


Fig. 2.— X-ray image of NGC 1566 (in center), accumulated by *Swift*/XRT from December 12, 2007 to November 2, 2023 with a 230 ks exposure time. The yellow contours in this image demonstrate the lack of X-ray jet-like structure, as well as minimal contamination by other point sources within 18". The closest next source is 21" (LSXPS J041956.5–545528 is marked with a green circle).

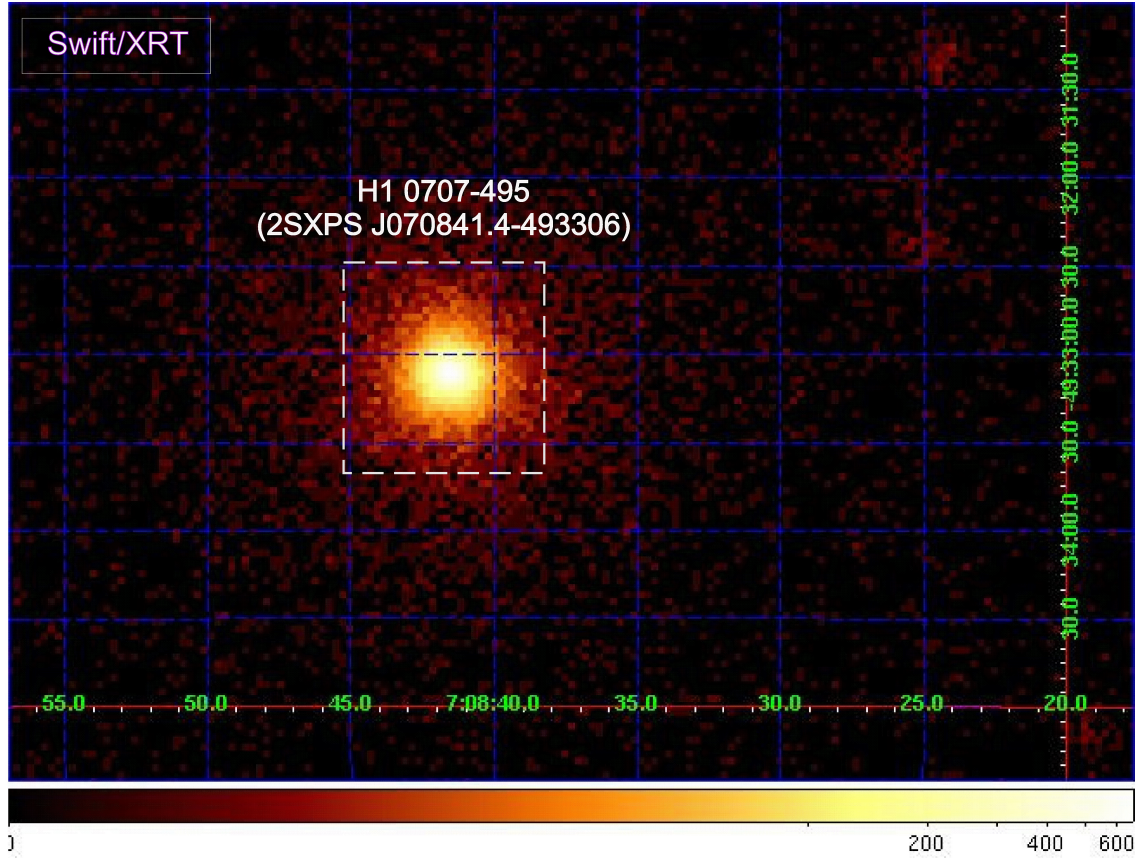


Fig. 3.— X-ray image of 1H 0707–495 (2SXPS J070841.4-493306 – according to the *Swift* catalog), accumulated from April 3, 2010 to April 30, 2018 with a 160 ks exposure time. The dashed square with a side of 6.3' (160 pixels) in the SDSS J0752 image demonstrates the absence of other nearby objects in the 1.3' field of view. The next closest source is 166" away (outside the image).



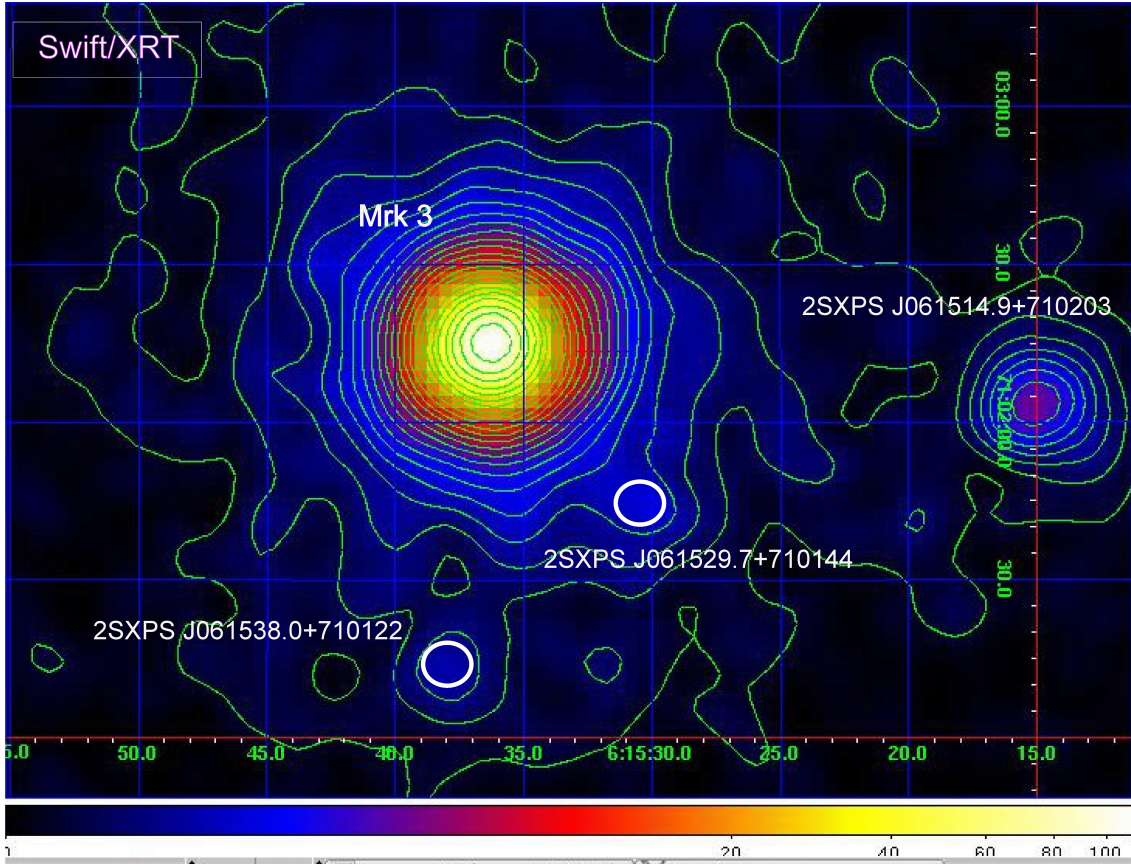


Fig. 4.— X-ray image of Mrk 3 (in center), accumulated by *Swift*/XRT from March 21, 2006 to April 20, 2015 with a 91 ks exposure time. The green contours in this image demonstrate the lack of X-ray jet-like structure around Mrk 3, as well as minimal contamination by other point sources within 18" of the source environment. The closest next source is 21" (LSXPS J041956.5–545528 is marked with a white circle).

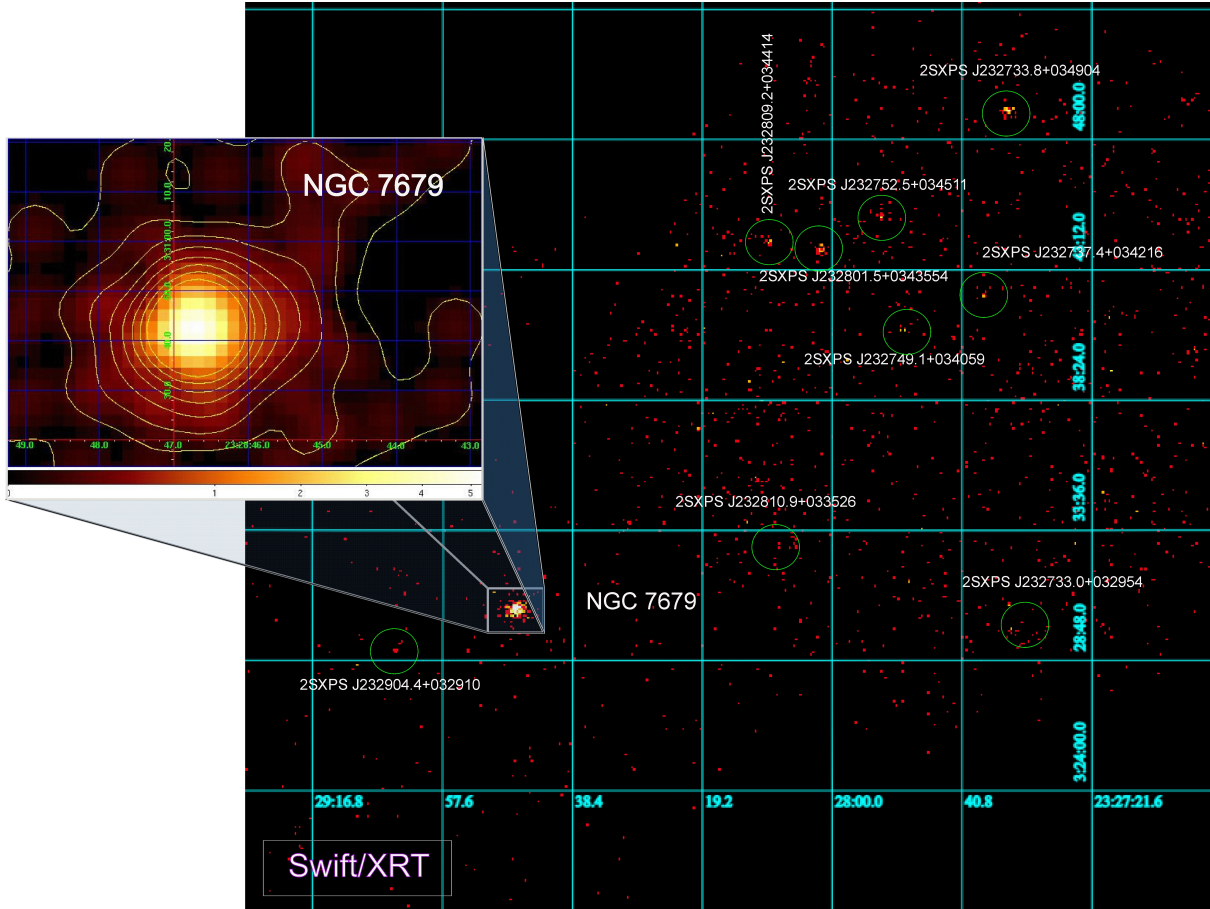


Fig. 5.— X-ray image of NGC 7679 (LSXPS J232846.7+033042 – according to the *Swift* catalog), accumulated from July 25, 2015 to October 6, 2017 with a 1.7 ks exposure time. The image segment highlighted with a gray square with a side of 6.3' (160 pixels) is also shown in more detail in the enlarged panel. Contour levels demonstrate the absence of X-ray jet (elongated) structure and minimal contamination from other point sources and diffuse radiation in the 1.3' field of view around NGC 7679. The next closest source is 2LSXPS J232904+032910, 279" away.

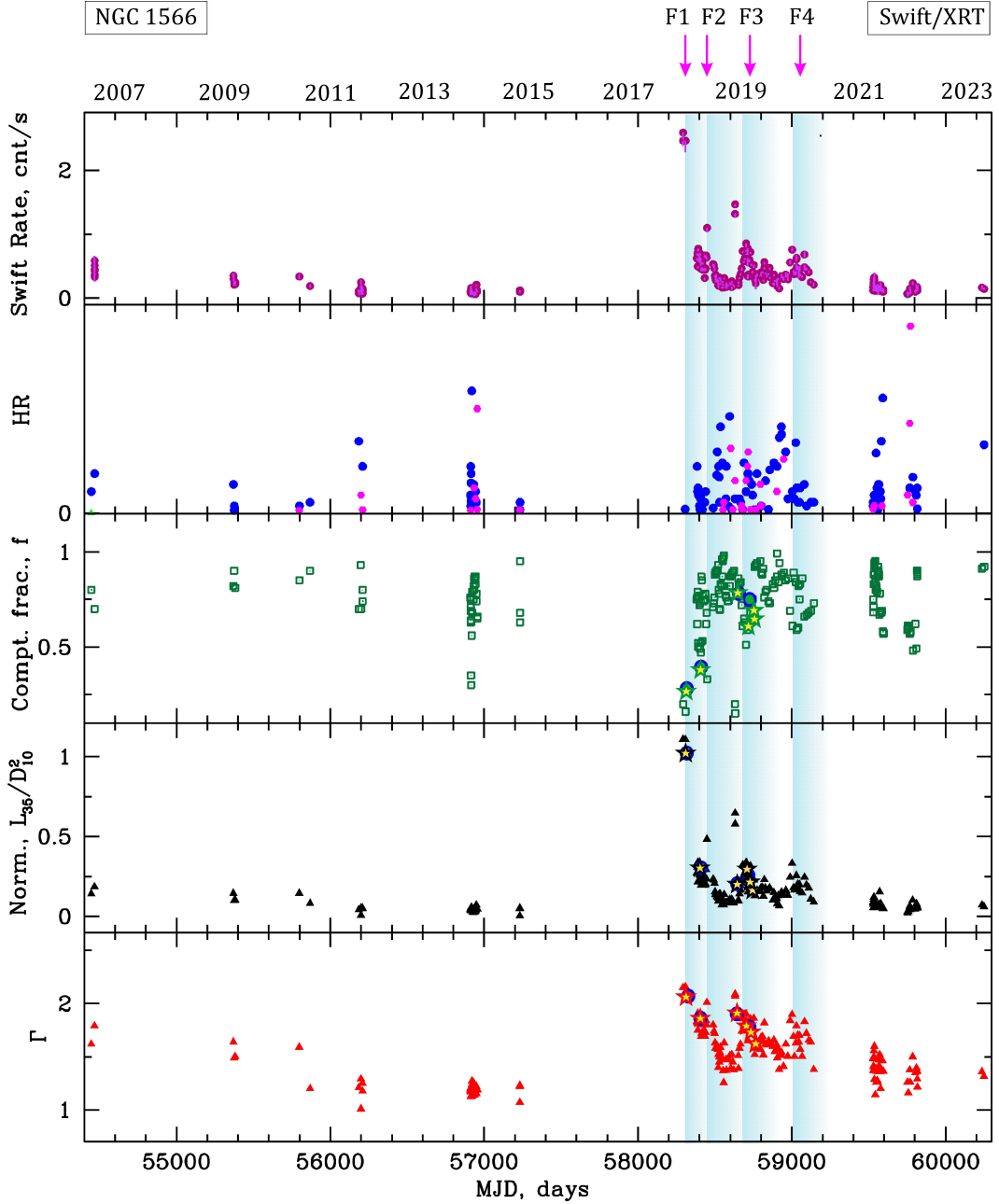


Fig. 6.— From top to bottom: evolution of the Swift/XRT count rate, hardness ratios HR1 and HR2 (blue and crimson points, respectively), Comptonized fraction  $f$ , and BMC normalization during 2007 and 2023 flare transition of NGC 1566. In the last bottom panel, we present an evolution of the photon index  $\Gamma = \alpha + 1$ . The decay phases of the flares are marked with blue vertical strips. The peak outburst times are indicated by the arrows at the top of the plot. For three bottom panels *NuSTAR* and *XMM-Newton* observations are indicated with stars and circle points, respectively.

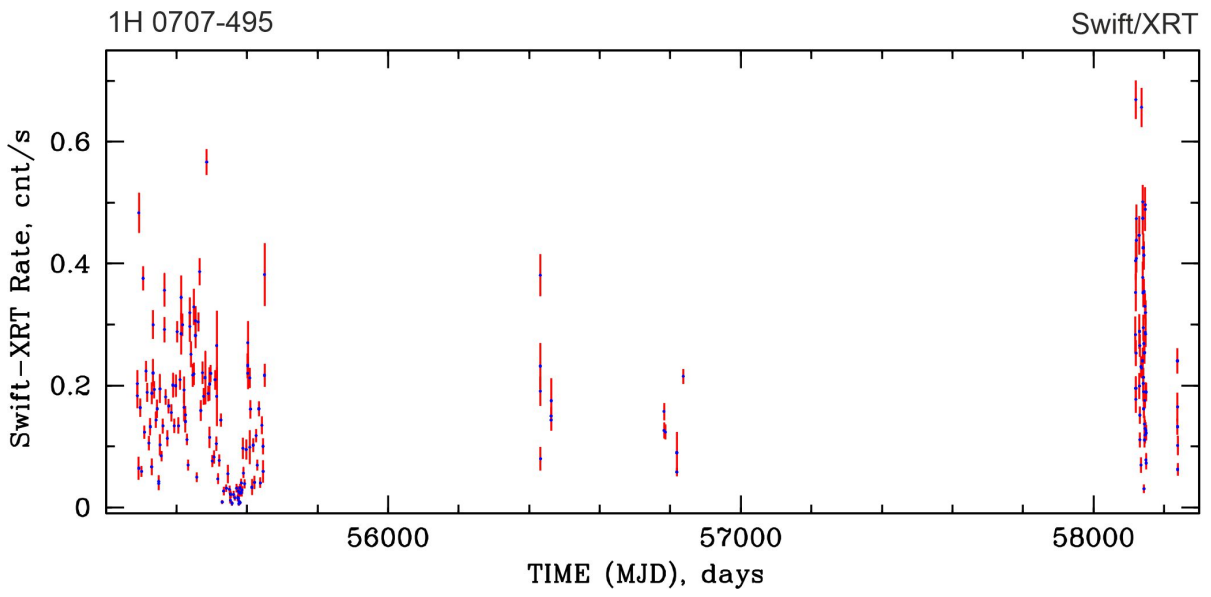


Fig. 7.— Evolution of the Swift/XRT count rate during 1996 – 2010 observations of 1H 0707–495.

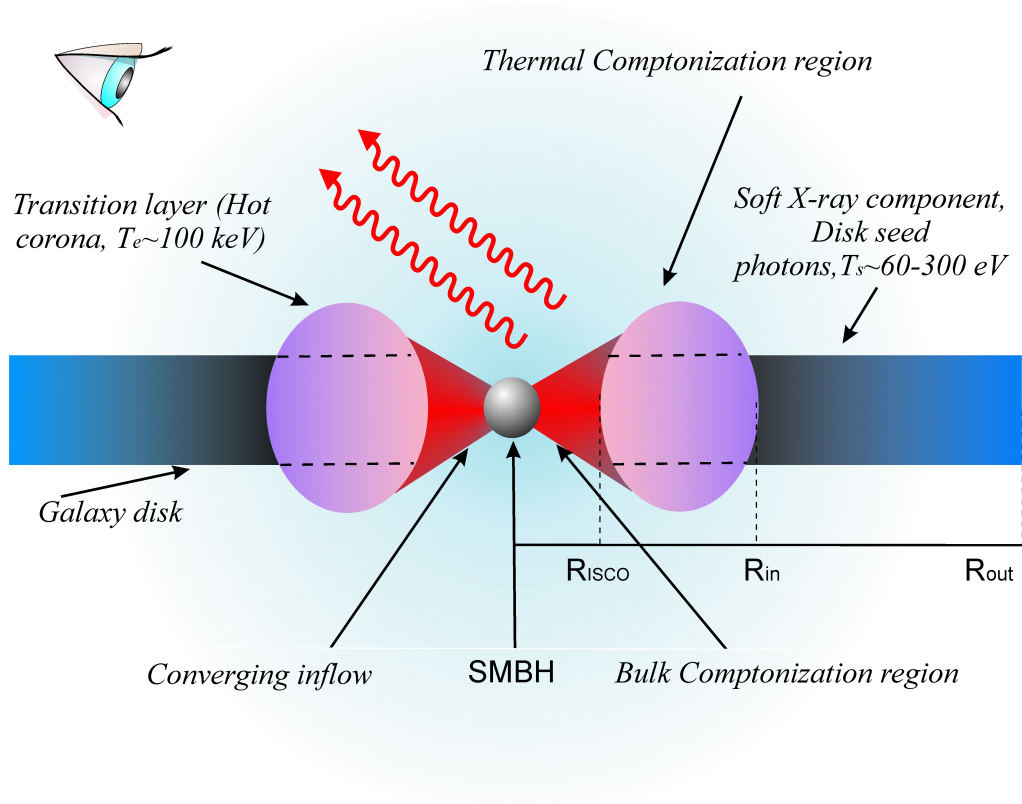


Fig. 8.— A suggested geometry for NGC 1566, 1H 0707, Mrk 3 and NGC 7679 sources. Disk soft photons are upscattered (Comptonized) off relatively hot plasma of the transition layer.



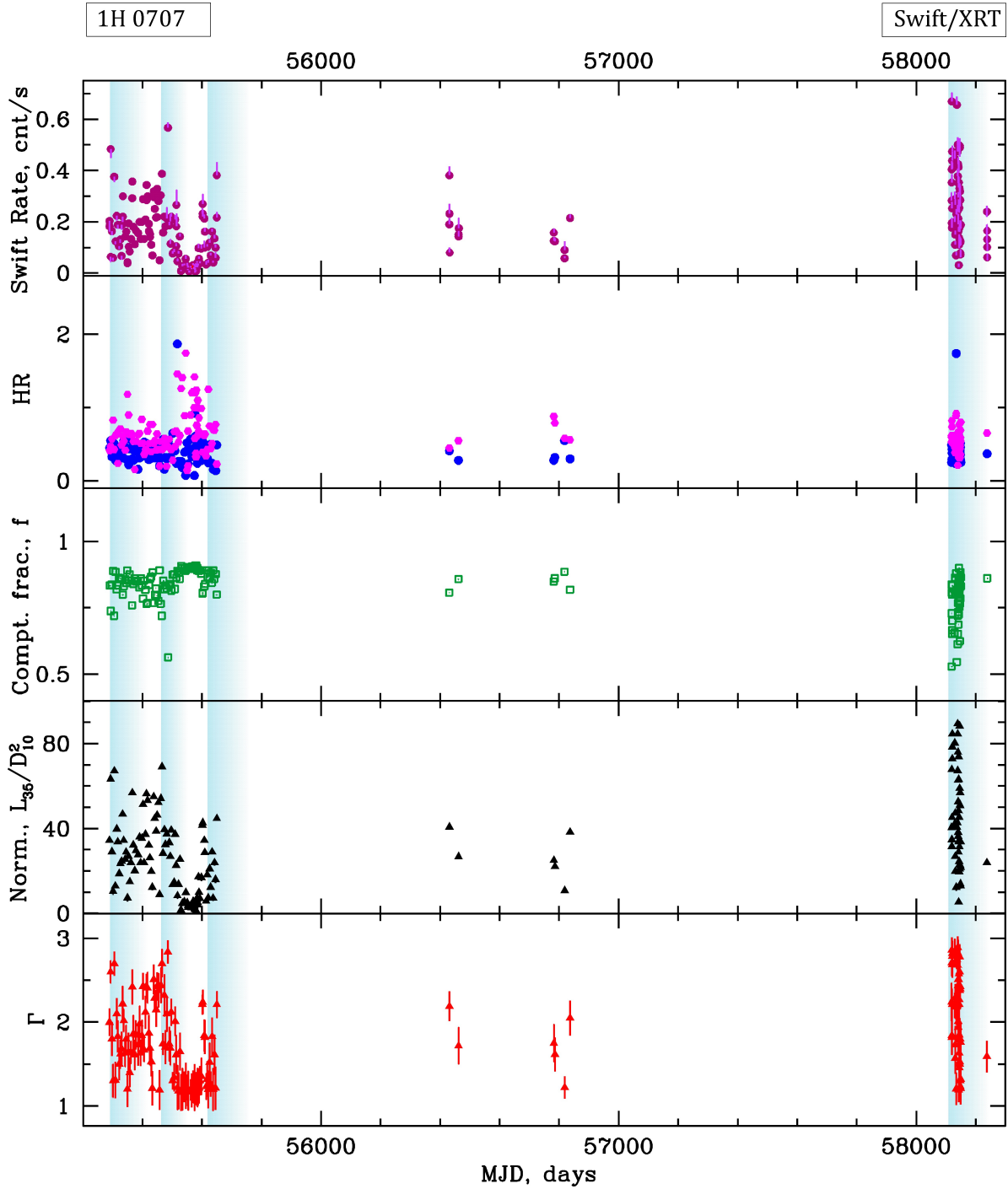


Fig. 9.— From top to bottom: evolution of the Swift/XRT count rate, hardness ratios HR1 and HR2 (blue and crimson points, respectively), Comptonized fraction  $f$ , and BMC normalization during 2010–2018 flare evatns of 1H 0707. In the last bottom panel, we present an evolution of the photon index  $\Gamma = \alpha + 1$ . The decay phases of the flares are marked with blue vertical strips.

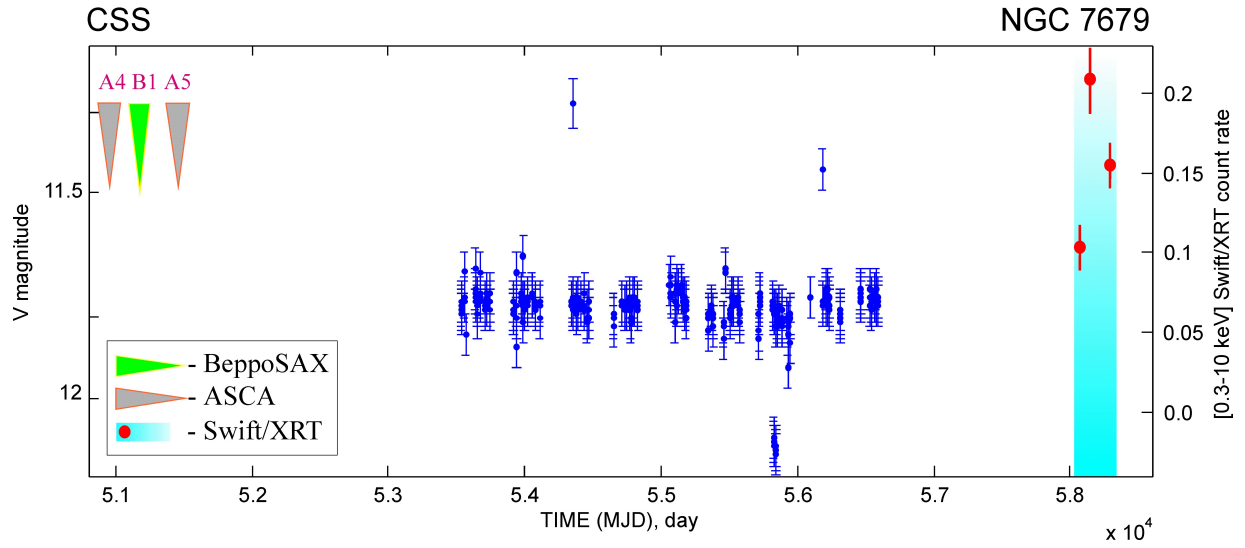


Fig. 10.— The distribution of NGC 7679 observations by *Swift*/XRT (bright blue vertical strip with red points), *BeppoSAX* (green arrow), and *ASCA* (grey arrows) is shown along with the CSS V-band light curve (blue points) , (see Tables 2 and 3).

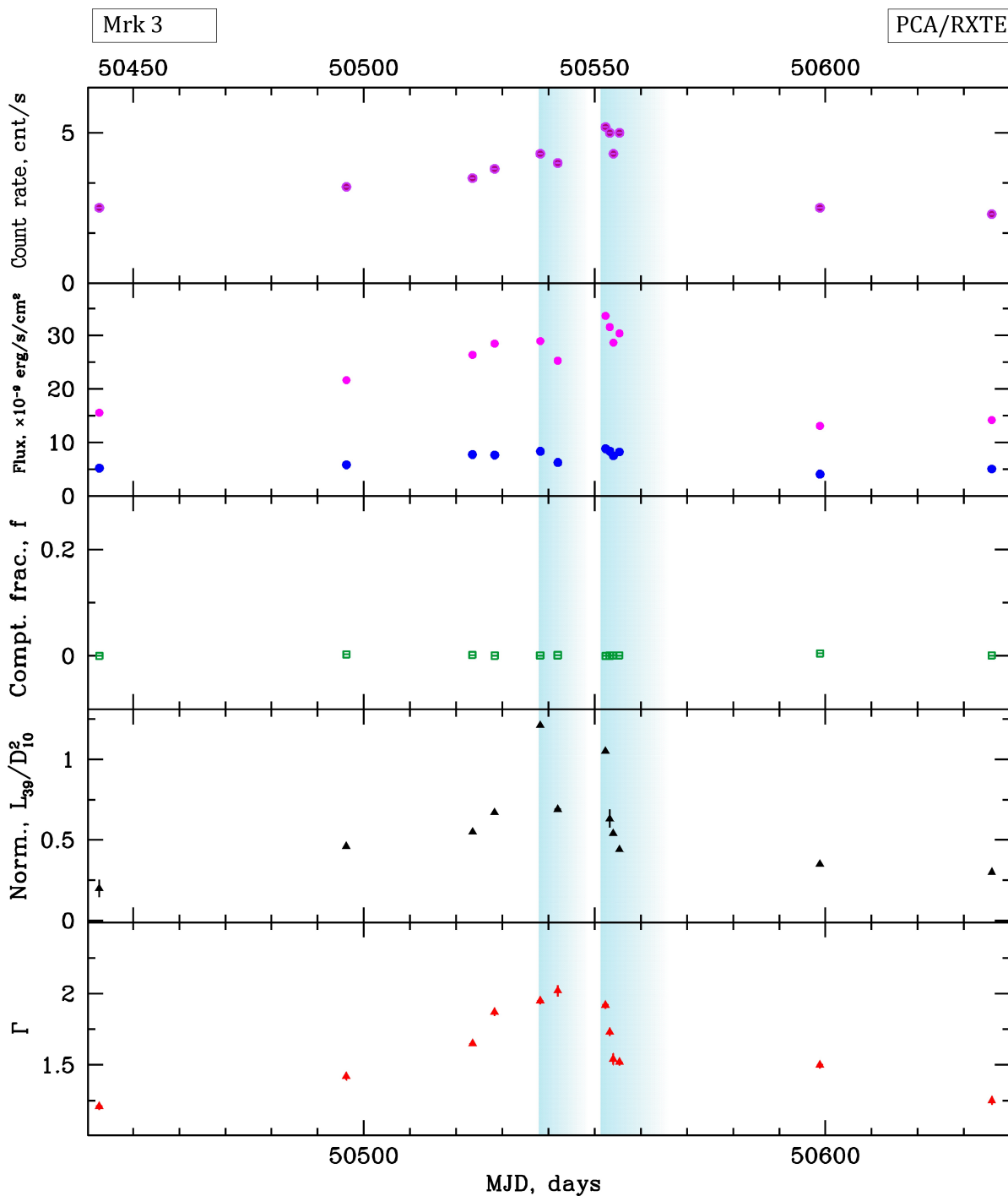


Fig. 11.— From top to bottom: evolution of the *RXTE*/PCA count rate, fluxes in 3–10 keV (blue points) and 10–20 keV (crimson points) bands, Comptonized fraction  $f$ , and BMC normalization during 1997–1997 flare events of Mrk 3. In the last bottom panel, we present an evolution of the photon index  $\Gamma = \alpha + 1$ . The decay phases of the flares are marked with blue vertical strips.

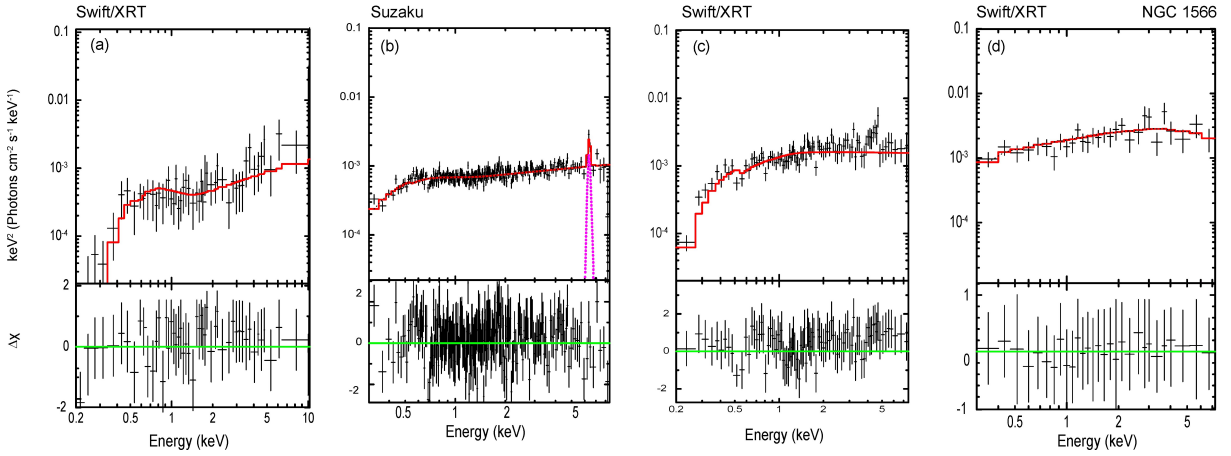


Fig. 12.— Four representative spectra of NGC 1566 from *Swift* data in units of  $E * F(E)$  with the best-fit modeling for the LHS (ID=00014916001, panel *a*), IS (ID=707002010, IS (ID=00014923002, panel *c*) and IS (ID=00035880003, panel *d*) states. The spectrum of NGC 1566 from *Suzanne* with the best-fit modeling for the LHS (ID=707002010, panel (b)). The data are denoted by crosses, while the spectral model is shown by a red histograms for each state. Bottom:  $\Delta\chi$  vs photon energy in keV.

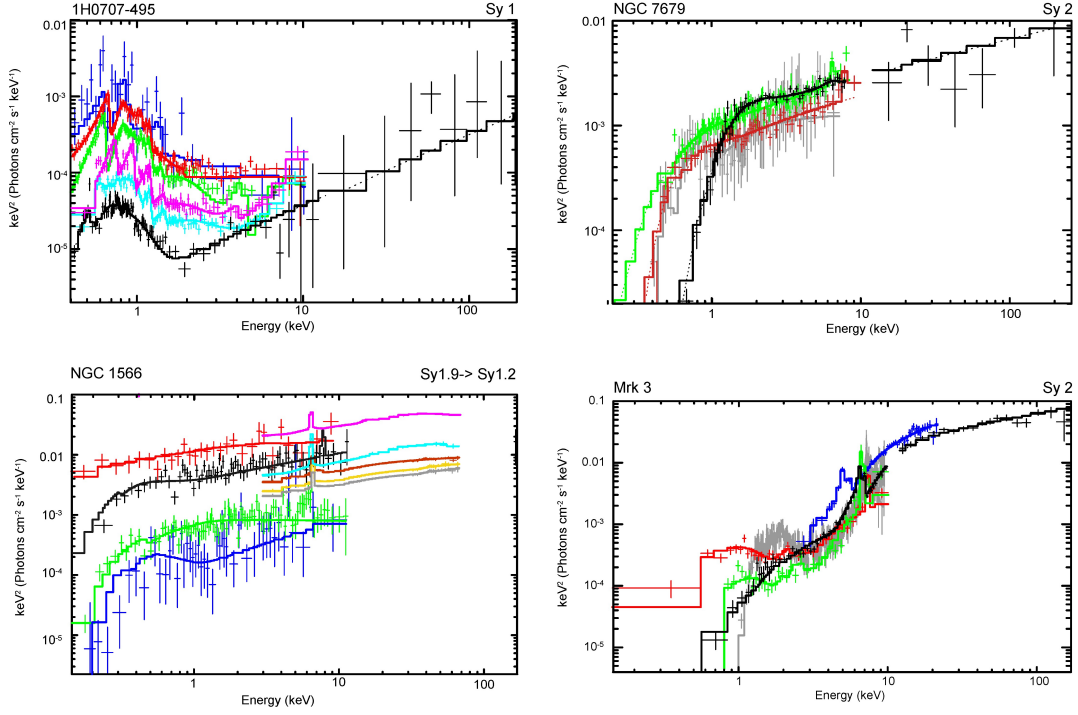


Fig. 13.— Representative  $E * F(E)$  spectral diagrams that are related to different spectral states for 1H 0707–495 (top left) using Suzaku observation 00091623 (black, LHS) combined with *RXTE*/HEXTE observation 20309010100 (black, LHS), *ASCA* observations 73043000 (brigh blue, IS), 73043000 (pink, IS), 763100 (green, IS), Swift observation 0090393 (red, IS) and Swift obs 0091623 (blue, HSS); NGC 1566 (bottom left) using *Swift* observations 0001496 (blue, LHS), 00014923 (green, LHS), 00031742 (black, IS), 00035880 (red, IS), and *NuSTAR* observations 80301601002 (pink, IS), 80401601002 (bright blue, IS), 80502606002 (brown, IS), 60501031004 (yellow, IS) and 60501031006 (grey, IS); NGC 7679 (top right) using 40631001 (black, LHS, from *BeppoSAX*), 00088108002 (grey, LHS, from *Swift*), 66019010 (red, HIMS, from *ASCA*), and 66019000 (green, IS, from *ASCA*) and Mrk 3 (bottom right) using *ASCA* observation 70002000 (LHS, red), 70002000 (LHS, red), Suzaku observation 709022010 (LHS, green), *RXTE* observation 20330-01-09-00 (blue, IS), *BeppoSAX* observation 50132002 (IS, black).

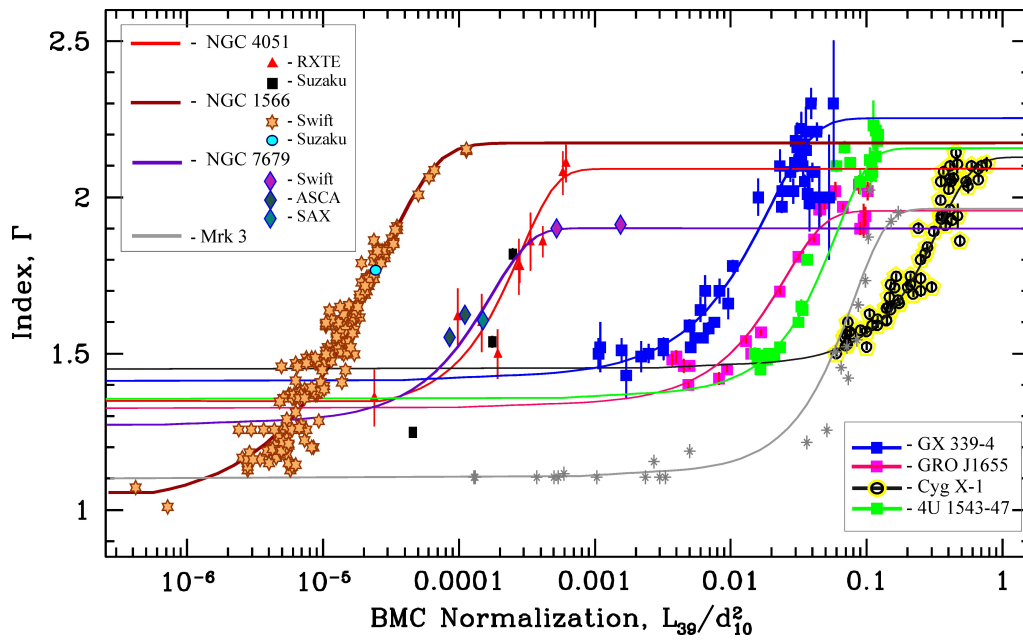


Fig. 14.— Scaling of photon index  $\Gamma$  for NGC 1566 (with brown line for target source) and NGC 7679 (with violet line for target source) with NGC 4051, GX 339–4, GRO J1655–40, Cyg X–1 and 4U 1543–47 as reference sources).

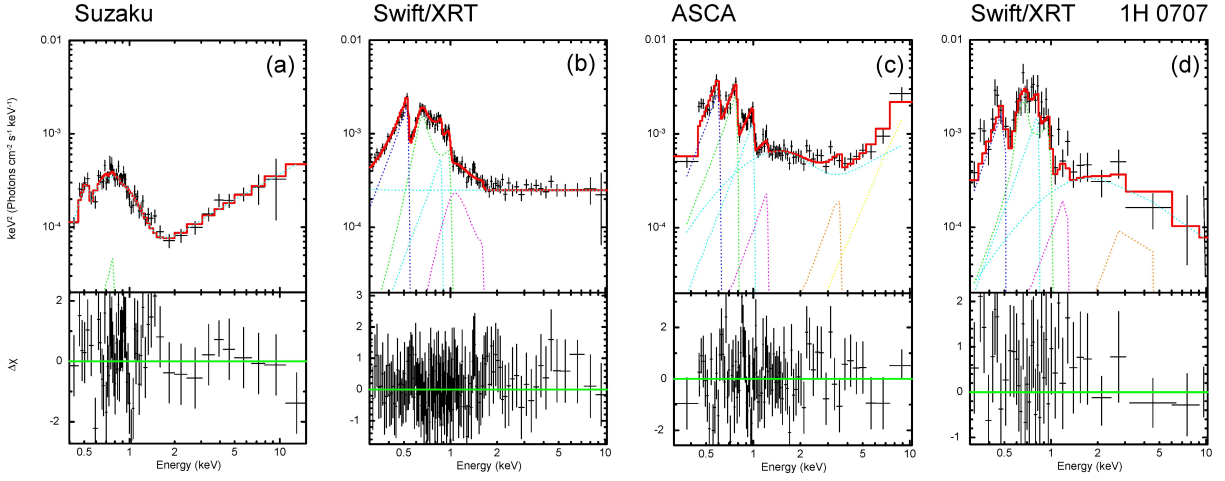


Fig. 15.— The best-fit spectrum of 1H 0707–495 in  $E * F(E)$  units during: (a) LHS using *Suzaku* observation 00091623; (b) (IS) using Swift observation 00091623002; (c) IS using ASCA observation 73043000 and (d) HSS using Swift observation 00080720048. The data are presented by crosses and the best-fit spectral model  $tbabs*(BMC+N*Laor)$  by red line. The Comptonization hump component is shown by the dotted sea-green line. To model the *Laor* line components, we used the N XVII (blue), O III (green), Fe XVII (bright blue), Ne X (pink), S XVI (orange), Fe I–XXII and Fe XXV/Fe XXVI  $K_{\alpha}$  (yellow) lines with energies of 0.5, 0.65, 0.85, 1.02, 2.9, 6.4, and 6.8 keV, respectively. Bottom:  $\Delta\chi$  vs photon energy in keV.

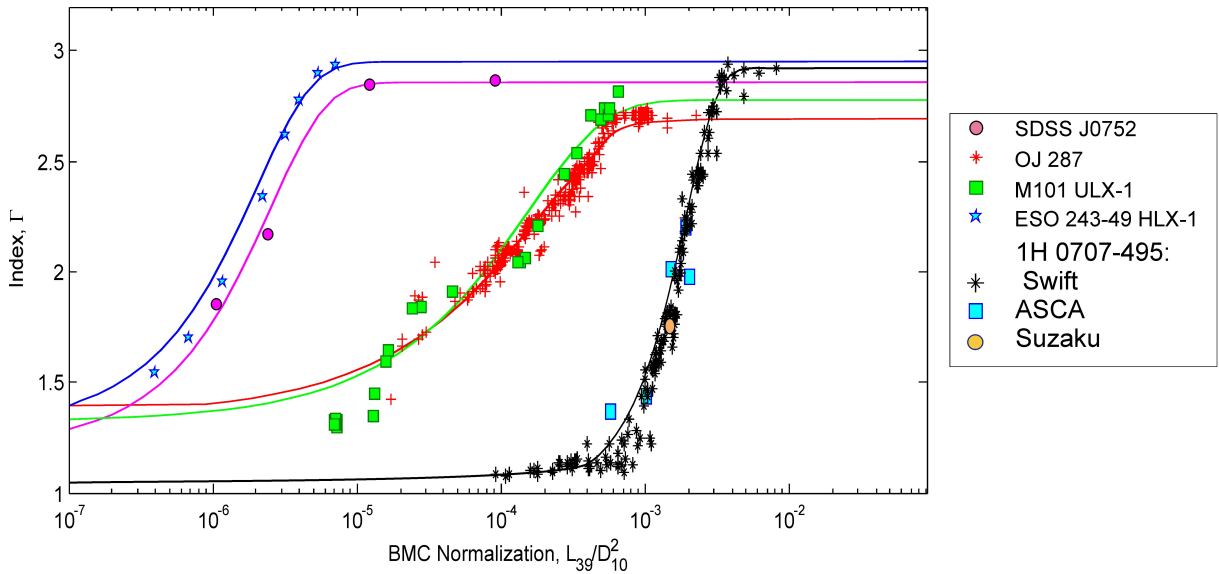


Fig. 16.— Scaling of photon index  $\Gamma$  for 1H 0707–495 (with black line for target source) and SDSS J0752, OJ 287 and M101 ULX–1 (as reference sources).

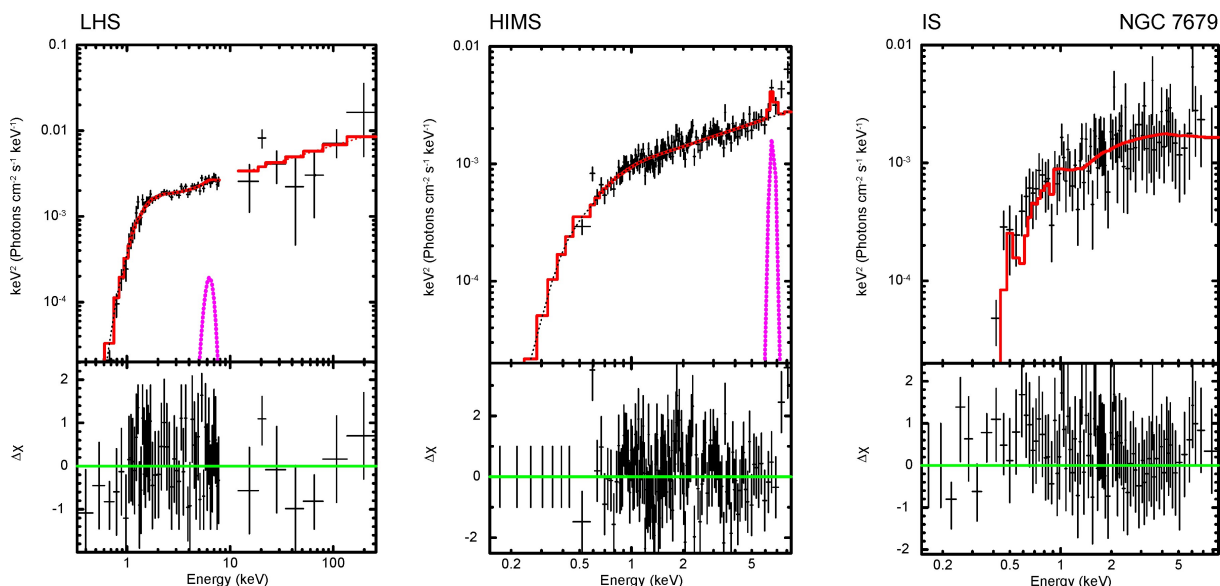


Fig. 17.— Three representative spectra of NGC 7679 with the best-fit modeling for the LHS (ID=40631001, left) using the *BeppoSAX* data, HIMS (ID=66019000, center) from *ASCA* and for the IS (ID=00088108002, right) from *Swift* in units of  $E * F(E)$  using the `tbabs*(bmc+gauss)` model, respectively. The data are denoted by crosses, while the spectral model is shown by a red histograms for each state. o model the line component, we used Fe XXV/Fe XXVI  $K_\alpha$  (pink) lines with energies of 6.7/6.9 keV. Bottom:  $\Delta\chi$  vs photon energy in keV.

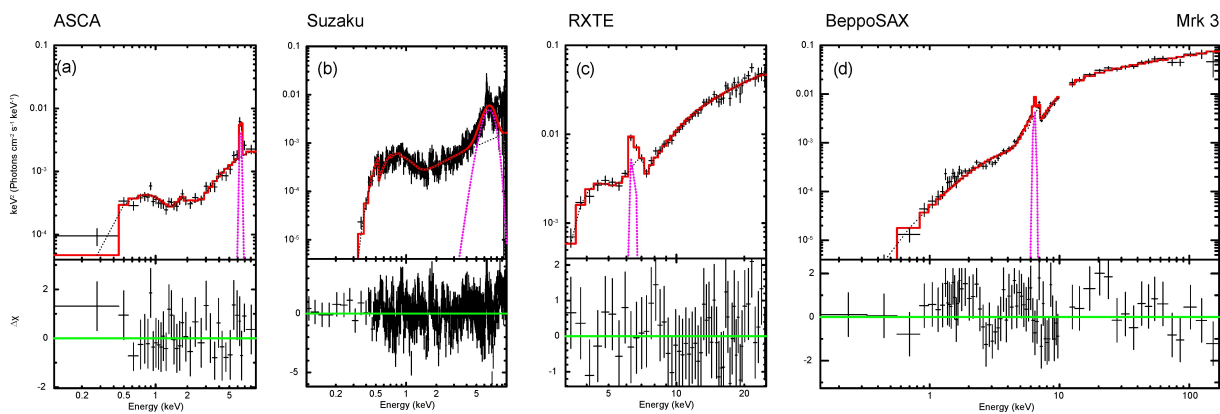


Fig. 18.— Four representative spectra of Mrk 3 in units of  $E * F(E)$  with the best-fit modeling for the LHS (*ASCA* observation with ID=70002000, panel *a*), IS (*Suzaku* observation with ID=100040010, panel *b*), IS (*RXTE* observation with ID=20330-01-09-00, panel *c*) and IS (*BeppoSAX* observation with ID=50132002, panel *d*) states. The data are denoted by crosses, while the spectral model is shown by a red histograms for each state. Bottom:  $\Delta\chi$  vs photon energy in keV.



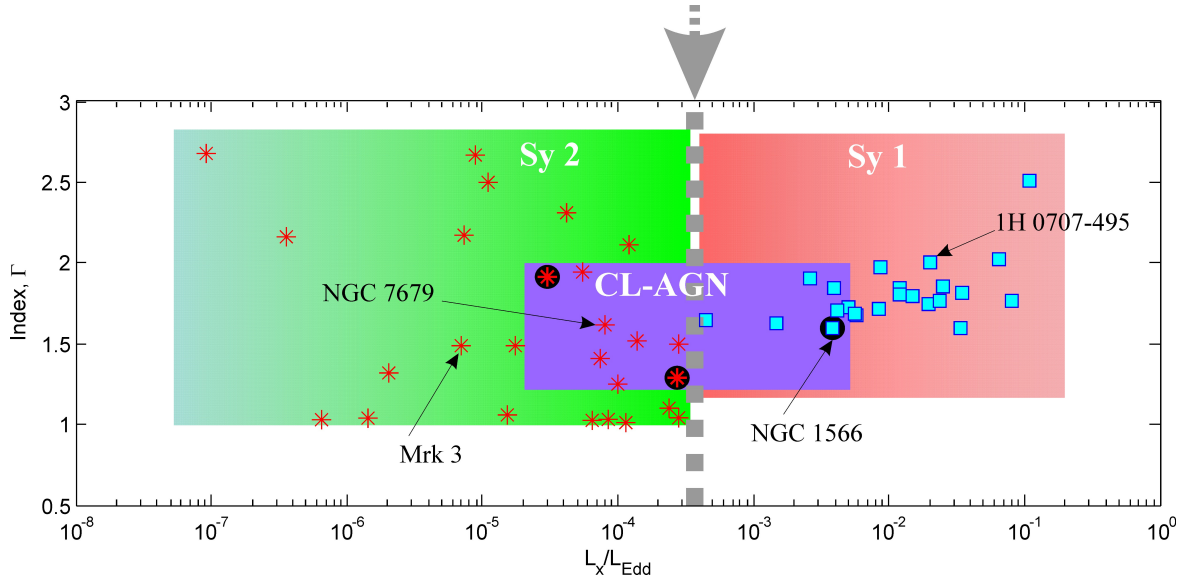


Fig. 19.— Photon index,  $\Gamma$  plotted versus  $L_x/L_{Edd}$  for Sy 1 (red box), Sy 2 (green box) and CL-AGN (violet box). The grey dotted arrow indicates the critical value of  $L_x/L_{Edd}$ , separating Sy1 and Sy2. It is evident that the CL-AGN box covers both the Sy1 and Sy2 AGN regions.

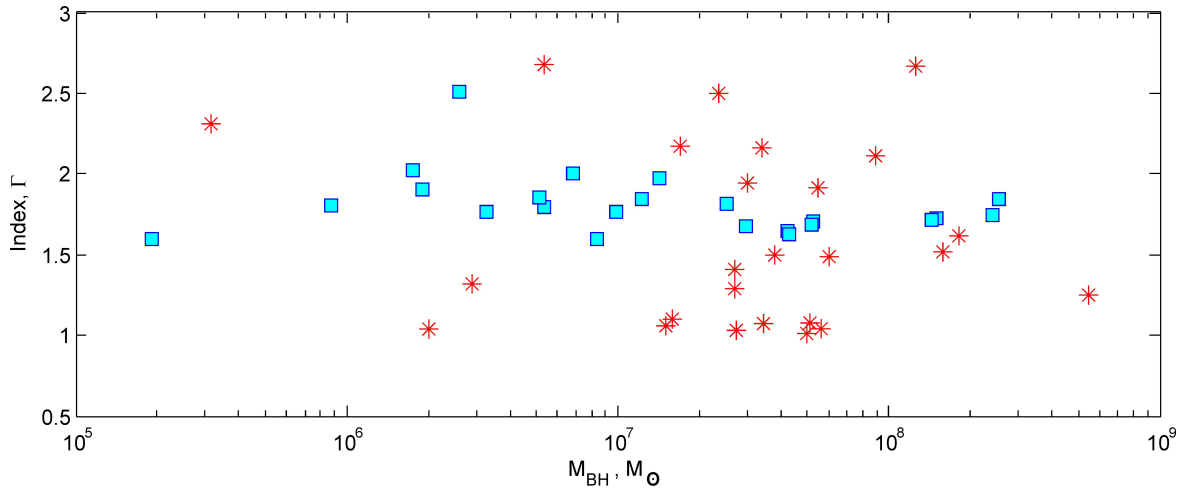


Fig. 20.— Photon index,  $\Gamma$  plotted versus a BH mass for Sy 1 (blue squares) and Sy 2 (red stars) AGNs.

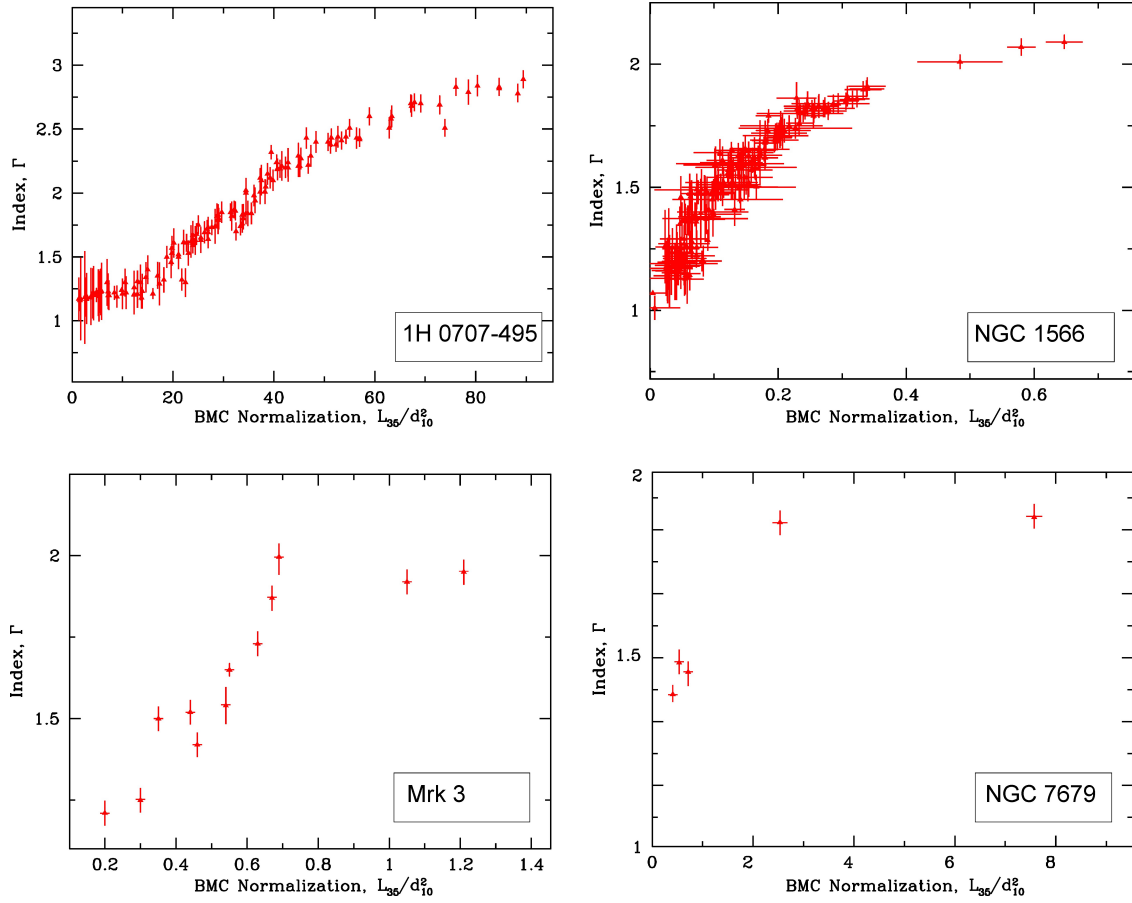


Fig. 21.— Photon index,  $\Gamma$  plotted versus BMC normalization (which is proportional to  $\dot{M}$ ) for 1H 0707 (top left panel), NGC 1566 (top right panel), Mrk 3 (bottom left panel) and NGC 7679 (bottom right panel).